Trailing edge bluntness noise reduction using porous treatments

Syamir Alihan Showkat Ali[a,b], Mahdi Azarpeyvand[b], Carlos R. Ilário da Silva[c]

[a]*School of Manufacturing Engineering, Universiti Malaysia Perlis, 02600, Arau, Perlis, Malaysia*
[b]*Department of Mechanical Engineering, University of Bristol, Bristol BS8 1TR, UK*
[c]*Embraer, São José dos Campos, 12227-901, Brazil*

Abstract

This paper provides an experimental investigation of the noise generated from a blunt flat plate and the possibility of the control of noise at source using porous trailing edges. The noise generation characteristics have been examined using a flat plate equipped with surface pressure transducers and far-field microphones and was performed in an anechoic open jet wind tunnel. Two types of porous materials with different porosities and permeability constants were tested. Simultaneous near-field and far-field noise measurements, as well as the boundary layer and wake flow measurements, have been carried out to better understand the effects of the porous treatment to the flow-field and the noise generation mechanism of the plate. Results have shown that the use of porous trailing edges can generally lead to the effective suppression of both the tonal noise, due to the vortex shedding from the blunt trailing edge and also the broadband noise of the plate. The level of the noise reduction was also found to be dependent on the porosity and permeability of the porous materials. The directivity patterns of the radiated noise have shown significant noise reduction at the vortex shedding frequencies. The flow measurement results have shown that the use of porous trailing edges leads to the reduction of flow acceleration over the blunt edges, and subsequently the delay and weakening of the vortex shedding. The results presented in this paper provide an impetus for further experimental and numerical studies on the use of porous treatments for the suppression of aerodynamically generated noise at source.

Keywords: porous material, turbulent flow interaction, noise reduction
2010 MSC: 00-01, 99-00

1. Introduction

Over the last two decades, a great deal of research has been directed toward the reduction of environmental noise exposure, in particular, the aviation noise from aircraft operations. With air travel continually rising, the effects of aircraft noise exposure have turned into a major public and global issue, which has direct economic impacts on the nations' gross domestic product. As a result, substantial research is directed by major aviation industries for the better understanding of the noise generation mechanism and development of tailored flow and

Email addresses: syamir.alihan@gmail.com (Syamir Alihan Showkat Ali), m.azarpeyvand@bristol.ac.uk (Mahdi Azarpeyvand), carlos.ilario@embraer.com.br (Carlos R. Ilário da Silva)

noise control methods for the development of new generation of quieter aircraft. The problem of radiated noise from bluff bodies, blunt edges and airfoils have been the subject of many experimental and numerical studies. A large number of studies have been carried out using different active and passive flow control methods, such as flow suction and blowing [1, 2], serrations [3–5], porous treatments [6–9], surface treatments [10], morphing [11], etc; for controlling the unsteady turbulent flows, improving aerodynamic performance of such device and reducing aerodynamically generated noise. The application of porous materials, in particular, for flow and thermal purposes has received substantial academic attention to better understand the physics and the underlying mechanisms of flow and noise control, particularly in the areas of fluid mechanics, aerospace, underwater vehicles, etc. In general, it has been shown that the application of porous materials for flow control in aerodynamic and aeroacoustic applications leads to robust control of flow-induced noise and vibrations, turbulence stabilization and significant aerodynamic improvement. In what follows, a comprehensive review of the fundamental studies of the porous material for noise reduction purposes and the significance of the porous surfaces on airfoils and bluff bodies applications are provided.

Substantial computational and experimental research has been directed towards the application of porous treatments for the reduction of airframe noise and airfoil self-noise. Choudhari and Khorrami [12] studied the application of porous treatments over a small fraction of the flap trailing-edge using the Reynolds-averaged Navier-Stokes simulations. The results had shown that porous treatments are able to modify the vortex initiation and roll-up turbulence structures from the flap side-edge and at high flap deflections, leading to airframe noise reduction. Furthermore, the use of porous treatments for slat noise reduction has been computationally studied by Khorrami and Choudhari [13]. The results have shown that by applying porous media over a small fraction of the slat area can lead to a significant reduction in the pressure fluctuations of about 20 dB in the vicinity of the treated surface. The reduction in the pressure fluctuations over the treated slat surface is associated with the reduction and the upward shift of the shedding frequency. Bohn [14] performed experimental studies to investigate the characteristics dependencies of edge-noise reduction over a flat plate trailing edge using porous materials with various flow resistivity and surface geometry. The study concluded that noise reduction can be attributed to the surface impedance of the trailing edge through an acoustic feedback mechanism. Fink and Bailey [15] studied the application of porous treatments on flow around the flap and slat of a high-lift device and showed that the turbulent broadband noise generated by the flap trailing edge and slat leading edge can be significantly reduced by about 2-3 dB, respectively. Revell *et al.* [16] investigated the effects of porous materials on airframe noise and it was shown that the porous treatments can significantly reduce the noise generation from the flap-side edges with a minimal aerodynamic penalty. The main reason for the noise reduction is believed to be due to the flow penetration and dissipation through the porous medium and porous surface impedance reduction. A similar study was performed by Angland *et al.* [17] on porous-treated flap side-edge and the results have shown that the turbulent shear stresses due to the vortex shedding were reduced significantly, which suggests the mitigation of the aerodynamic noise source at the trailing edge vicinity. The effects of comb-type edges on a flat plate and NACA0012 airfoil have been investigated by Herr [18] and showed that a significant reduction on the broadband trailing-edge noise of about 10 dB can be achieved using such edge treatments. The noise reduction mechanisms at the trailing edge are associated to the dampening of the turbulent

flow pressure fluctuations and hydrodynamic absorption in the porous medium. The impact of the flow interaction with different porous sections applied at the trailing edge of airfoils has been studied extensively by Geyer and Sarradj [19]. It was observed that a higher noise reduction was achieved using the larger porous sections and that the partially porous trailing edge leads to substantial noise reduction and owns better aerodynamic performance. The noise reduction obtained was elucidated to be caused by the hydrodynamic damping effect and changes in the energy content of the turbulence structures of the porous treatments.

There is a relatively large body of literature on the application of porous materials for controlling the flow around bluff bodies and blunt edges and some investigation on its potential effect on noise reduction. Liu *et al.* [20] have carried out an unsteady fluid dynamics simulation on the implementation of a porous coating on round cylinders. The results have shown that the porous treatments can significantly alter the near-wake flow structures and change the energy content near the cylinder by delaying the recirculation zone, which results in a significant noise reduction of about 20 dB at the vortex shedding frequencies. More recently, Liu *et al.* [21] have performed a comprehensive study on the application of porous coatings for reducing the aerodynamic noise from cylinders in tandem. The unsteady simulation results have shown that a significant reduction of about 15 dB in the overall sound pressure level can be achieved using the porous coatings and this was shown to be due to the gap flow stabilization and the reduction of the turbulent kinetic energy on the rear cylinder. Moreover, Bae *et al.* [22] have investigated the effect of porous treatments on the noise generated from a flat plate with a blunt trailing-edge using the incompressible large eddy simulation (LES) and linearized perturbed compressible equations (LPCE). Results show that the porous surface is capable of reducing the far-field noise by up to 13 dB at the fundamental vortex shedding peak, which might be due to the suppression of the surface pressure fluctuations in the vicinity of the trailing edge and the reduction in the surface pressure spatial correlation. Koha *et al.* [22] performed LES-based numerical simulations on the blunt trailing-edge and it was shown that the implementation of porous treatments can lead to the reduction of the sound pressure level at the vortex shedding frequency by up to 10 dB. In a later study, Koha *et al.* [23] showed that a significant reduction in the vortex shedding tonal noise can be achieved using porous trailing edges, leading to a reduction of the overall sound pressure level of about 11 dB. It was also found that the acoustic attenuation is influenced by the reduction in the flow acceleration in the near-wake region of the trailing edge. Seong *et al.* [24] have studied the impact of variable porosity and permeability on trailing-edge noise numerically and found that the overall sound pressure level of porous treated cases is reduced in the range of 11-12 dB at the vortex shedding tonal peaks. In addition to the CFD simulations, very recent experimental investigations by Showkat Ali *et al.* [6] have also shown that the proper utilization of porous trailing edge can, to a great extent, suppress the vortex shedding from the trailing-edge, reduce the energy content of the low-frequency boundary layer structures and attenuate the vortex shedding frequency. It was also shown that a significant reduction of the spanwise coherence of the large coherent structures can be achieved using the highly permeable surfaces [7]. Several mechanisms related to the flow and porous interaction were identified as the potential factors for the break-up of large coherent structures, suppression of vortex shedding, reduction in surface pressure fluctuations, etc, such as the 'flow penetration into the porous medium', 'hydrodynamic absorption', 'quasi-periodic recirculating flow field inside the porous medium', etc [6, 7].

Despite a large body of literature on better understating of flow interaction with porous surfaces and permeable media, particularly for aeroacoustic applications, very few high-quality experiments have been carried out to relate the far-field noise reduction to the near-field flow characteristics. As reviewed above, the recent experimental investigations on the development of boundary layer over permeable surfaces [6, 7] have shown the effectiveness of such treatments for the manipulation of the boundary layer, break-up of coherent structures, reduction of the energy content of the boundary layer and wake flow structures, delay or suppression of vortex shedding, etc. However, the issue of radiated noise and its links to these phenomena has not received much experimental attention. While our previous study [6] focused on the emergence of the internal hydrodynamic field and the near-field flow, the current paper addresses the issue of far-field noise reduction and mechanism leading to the suppression of vortex shedding noise. The present work aims to provide a comprehensive study of noise generation and control from a long flat plate with a blunt trailing edge by conducting a series of near-field flow and far-field noise measurements. The effectiveness of the trailing edge porous treatments for noise abatement at source will be investigated and the underlying mechanisms will be studied. The experimental setup and wind tunnel tests are described in Sec. 2. The results concerning the far-field noise are described in Sec. 3, and the potential mechanisms governing the noise generation from blunt trailing edges with and without porous treatments are detailed in Sec. 4.

2. Measurement Setup

The flow and far-field noise measurements have been carried out for a blunt flat plate with solid and porous trailing edges in the low turbulence wind tunnel and the aeroacoustic facilities of the University of Bristol. The low turbulence wind tunnel is a closed-return type tunnel with an octagonal test section of 0.8 m length, 0.6 m width and 1 m height and has a contraction ratio of 12:1. The wind tunnel is capable of a maximum flow speed of 100 m/s, with a turbulence intensity of 0.05 % at 20 m/s. The open jet anechoic wind tunnel is a closed-loop feedback type tunnel with an external dimension of 7.9 m length, 5.0 m width and 4.6 m height, including the surrounding acoustic walls. The nozzle has a dimension of 0.6 m width and 0.2 m height, with a contraction ratio of 27:0:1. The nozzle is capable of a maximum reliable speed of 100 m/s at the contraction nozzle exit and with a turbulence intensity of 0.2 % at 30 m/s. The nozzle used in the present studies has the same width-to-height aspect ratio to that of [25, 26]. The flow and noise data have been collected for the flow velocities of up to U_∞=60 m/s, corresponding to the plate thickness-based Reynolds number of 1.5×10^6.

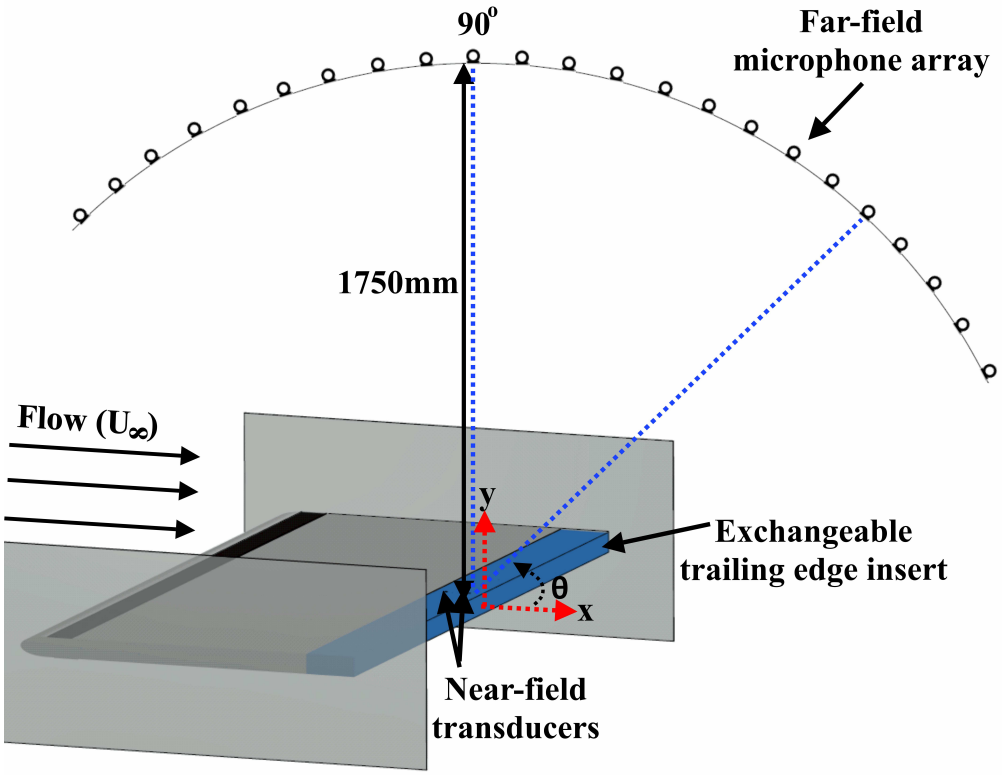

Figure 1: The schematic of the flat plate setup used for the acoustic measurements (not to scale).

2.1. Flat plate model design

The schematic of the flat plate model is shown in Fig. 1. The flat plate has a streamwise length of L_x= 0.35 m and width of L_z= 0.6 m, with an elliptical leading edge to prevent flow separation at the beginning of the plate. The plate was designed with a thickness of h =0.02 m, where the bluntness ratio (h/δ^*, δ^* is the boundary layer displacement thickness at the trailing-edge) was found to be larger than 0.3 [27], ensuring the presence of vortex shedding. To ensure a well-developed turbulent flow before the porous section, a 0.025 mm wide sand trip was applied just after the leading edge, on both sides of the plate, with a thickness of approximately 600 μm and grit roughness of 80, corresponding to the average roughness of 1.8 μm. The porous section is placed at the trailing edge with a length and width of 0.05 m and 0.6 m, respectively. Rectangular side plates of dimension 0.45 m by 0.2 m, with sharpened trailing edges with an angle of 20° were mounted on the nozzle. The coordinate system (x, y, z) is placed at the centre of the trailing edge. The y' axis defined as y'=$y - h/2$=0, is introduced on the top surface of the plate, which is used to describe the boundary layer results in Sec. 4.1.

2.2. Porous samples characteristics

Two uncompressed metal foams with the PPI (pores per inch) values of 25 and 80 have been selected for this study. The porosity (φ) and permeability (κ) of the material are the

properties of major importance that will significantly affect the flow structures [6, 20, 28, 29] and, therefore, will be used to describe the porous samples studied here. Additionally, the surface roughness (Ra) of the open-pore porous substrates are also being investigated as another parameter which can affect the flow structures [7]. It is widely accepted [7] that the permeability and the surface roughness is nearly directly proportional to the porosity of the material. The porosity (φ), the air flow permeability (κ) and the surface roughness (Ra) of the porous materials have been measured and are further discussed in the next sub-subsections.

2.2.1. Porosity analysis

The porosity of the porous samples was measured using a Nikon XT H 320 LC Computed Tomography (CT) scanning and the data obtained were then visualized and analyzed using the Volume Graphics (VGStudio MAX 2.2) software. The data segmentation probability threshold value is set to 1.0 for the computation of the porosity value and the uncertainty of the porosity values was found to be within 2%. The porosity (φ), is calculated from $\varphi = V_V/V_T$, where V_V is the volume of void space and V_T corresponds to the total volume of the sample. The CT scanning images of the porous structure are shown in Fig. 2. The porosity values for the porous 25 PPI and 80 PPI samples are found to be 90.92 % and 74.76 %, respectively.

2.2.2. Permeability analysis

The permeability of each porous sample was measured using a permeability test rig over a wide range of Darcy velocities. The test rig was made of a 2.5 m square cross-section long tube, equipped with several static and total pressure measurement points. The porous samples used for the permeability tests consist of a cross-section of 0.08 $\times$ 0.08 m and thickness of 0.01 m, installed 1.2 m from the inlet of the long permeability test-rig. The pressure drop across the porous samples acquired from the static pressure taps was computed using the MicroDaq Smart Pressure Scanner 32C with a sampling frequency of 500 Hz for 60 s. The uncertainty of the permeability measurements was found to be within 3%-5%. The permeability (κ) can be found using Dupuit-Forchheimer equation [30] from $\triangle p/t = \mu/\kappa\nu_D + \rho C\nu_D^2$, where $\triangle p$ is the pressure drop across the sample, t is the sample thickness, ρ is fluid density, C is the inertial loss, ν_D is the Darcian velocity, defined as the volume flow rate divided by cross-sectional area of sample. The permeability values for the porous 25 PPI and 80 PPI samples are found to be 8.2$\times$ 10^{-8} m^2 and 7.7$\times$ 10^{-9} m^2, respectively.

2.2.3. Surface roughness analysis

The surface roughness of the porous samples was measured using a non-contact profilometer Scantron Proscan 2100 and the data obtained were analyzed using the Proform software module. The laser profilometer's scanning operation was conducted over a 0.003 m by 0.003 m area of the porous samples, with the thickness of 0.001 m in order to acquire higher magnification results. The roughness of each porous surface was characterized by calculating the average roughness parameter or the arithmetical mean height (Ra) of the porous structure. The measurements were repeated for three times, and have been proven to be reproducible, with the uncertainty value of less than 1% with a 95% confidence level based on the method proposed by Efron [31]. The Ra values can be calculated from $R_a = 1/L_s \sum_{i=1}^{L_s} |y_i|$, where

L_s is the the sampling length and y_i is the variation of the vertical distance from the mean surface line to the i^{th} data point over the scanned area. The average roughness values the for porous 25 PPI and 80 PPI are found to be 1922 μm and 212 μm, respectively.

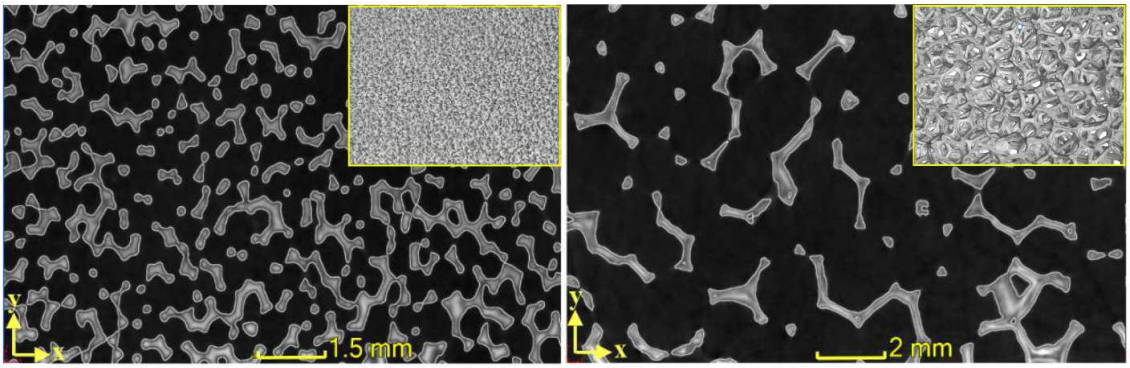

Figure 2: The CT scanning images of the porous structure.

2.3. Acoustic measurements and instrumentations

The layout of the experimental setup for the aeroacoustic measurements is shown in Fig. 1. An array of 23 GRAS 40PL free-field microphones, with a dynamic range of 142 dB, placed 1.75 m from the plate trailing edge has been used, as shown in Fig. 1. The GRAS 40PL microphones exhibit a flat frequency response, with a variation of $\pm$1 dB for frequencies from 10 Hz to 10 kHz, which covers the frequency range of interest in the present study. The microphone array in the anechoic chamber covers the polar angle range of 25° to 135°, with a regular interval of 5°. The polar angle θ is defined with respect to the flow direction, see Fig. 1. enable near-field to far-field analysis, two flush mounted FG-23329-P07 transducers were installed at the trailing edge section. Given the intrusive nature of the unsteady pressure measurement using miniature transducers inside the porous material, special care was taken to minimize any damage to the porous material structure and to avoid any flow interaction with the transducer and the cables. In order to avoid pressure attenuation at high frequencies, the transducers were placed inside a 3D printed capsule, with a pinhole mask of 0.4 mm diameter [32]. The geometrical dimensions of the pinhole configuration are chosen from a series of tests to ensure that the resonance frequency associated with the pinhole design does not affect the measurements within the frequency range of interest ($f \leqslant$ 10 kHz). The pinhole diameter is close to that of the diameter range suggested by Gravante [33]. The near-field and far-field data have been acquired using a National Instrument PXIe-4499 and the measurements have been carried out with a sampling frequency f_s of 2^{16} Hz and measurement time of 32 s. The pressure measurement data obtained give an absolute uncertainty of $\pm$0.5 dB with 99% of confidence level. The transducers are placed in the streamwise direction, at upstream of the trailing-edge section (x/h=-0.19) and at the end of the trailing-edge section (x/h=-0.35). The surface pressure transducer along with the hot-wire probe was used simultaneously to measure the boundary layer velocity-pressure correlation. Moreover, the surface pressure transducer along with the far-field transducer was

used simultaneously for the measurement of the coherence between the near-field boundary layer pressure exerted on the plate trailing edge and the far-field noise.

2.4. Particle Image Velocimetry setup

The time-averaged flow quantities of the blunt trailing-edge configuration, with and without the porous treatments were obtained using a two-component particle image velocimetry (PIV) system. The flow was seeded with mixed polyethylene glycol 80 tracer particles with a mean diameter of 1-5 μm. The tracers were illuminated by a 1 mm laser sheet thickness using a dual-cavity laser of 200 mJ Nd:YAG with a wavelength of 532 nm and repetition rate of 15 Hz. In order to obtain a maximum amount of tracer particles in the interrogation window, the time interval between each snapshot was set to 25 μs. The snapshots of the particles during illumination were captured by a FlowSense 4 MP CCD camera at the same time as the laser pulses, where the snapshots consist of two images containing the specific particle positioning. The uncertainty is measured by considering the uncertainty in the subpixel displacements [34] and was found to be below 1%. The statistical turbulent flow quantities were computed using a total number of 1600 image pairs with a resolution of 2048 $\times$ 2048 pixels for each case. The measurements were carried out for a field view of 158 mm $\times$ 158 mm, corresponding to a domain of 7.9 h $\times$ 7.9 h in both the streamwise and vertical directions. The iterative window correlation process yields a final interrogation window size of 16 $\times$ 16 pixels with an overlap of 50 %, producing a vector spacing of 1.23 mm.

2.5. Hot-wire anemometry setup

The boundary layer measurements were performed using a single hot-wire Dantec 55P16 probe, with a platinum-plated tungsten wire of 5 μm diameter and 1.25 mm length, and cross hot-wire Dantec 55P51 probes with 5 μm diameter and 3 mm length platinum-plated tungsten wires. The single and cross hot-wire probes have a length-to-diameter (l/d) ratio of 250 and 600, respectively, which provides adequate sensitivity in measuring the mean and fluctuating velocity with minimal thermal effects [35] and good spatial resolution. The data obtained were low-pass filtered using the Dantec StramlinePro frame with CTA91C10 modules with a corner frequency of 30 kHz and with an overheat ratio of 0.8 [36]. The probes were calibrated using the Dantec 54H10 type calibrator, before and after each measurement. The data have been collected using a National Instrument PXle-4499, with a sampling frequency of $f_s = 2^{16}$ Hz. The hot-wire signals were recorded for 16 s at each measurement locations. In order to ensure repeatability of the measurements, the boundary layer tests were repeated three times. The uncertainty of the velocity signals, computed using the manufacturer's method [36], was found to be within 1%. The hot-wire probes were moved around in the flow using a two-axis ($x - y$) ThorLabs LTS300M traverse system, which covers a 300 mm by 300 mm measurement domain in the streamwise and vertical directions, with a minimum positioning accuracy of ± 5 μm.

3. Aeroacoustic results

In this paper, the noise control mechanisms related to the flow-porous interaction have been investigated from both the aeroacoustic and aerodynamic points of view. This section is concerned with the far-field noise measurement from the blunt flat plate test rig and the

effect of the two porous treatment on the radiated noise. In what follows, a comprehensive investigation of the far-field noise, the directivity of the radiated sound and the near-field to far-field analysis is provided.

3.1. Far-field noise results

The sound pressure level (SPL) as a function of the Strouhal number ($St = fh/U_\infty$) obtained from the far-field microphones located at the polar angles of θ=45°, 60°, 90° and 120°, and flow velocity of U_∞=30 m/s are shown in Fig. 3. The sound pressure level (SPL) spectrum can be calculated from SPL = $20 \cdot \log10\ (P_{rms}/P_{ref})$, where P_{rms} is the root-mean-square of the acoustic pressure and P_{ref} is the reference pressure at 20 μPa. In order to estimate the energy content at different frequencies, the Welch power spectral density [37] of the pressure fluctuations has been carried out. The power spectrum with a Hamming window function was performed on the time-domain pressure data for segments of equal length with 50 % overlap, which provides us with a frequency resolution of 32 Hz. The power spectrum of the acoustic pressure signal is corrected to a reference distance of 1 m. The noise radiated from the plate is well above the background noise level for all frequencies of interest.

The results show the existence of a tonal peak at $St \approx 0.2$ at all microphone locations for the solid trailing edge case. This peak corresponds to the fundamental vortex shedding peak, which is similar to the surface pressure results reported in [6]. The results also have shown the emergence of a double vortex shedding peak at around the fundamental shedding frequency ($St \approx 0.2$) in the case of the solid trailing edge, indicating the existence of two types of vortical structures in the wake region. In the case of porous 80 PPI, it is observed that there is a consistent reduction of the vortex shedding tonal peaks in the noise spectra at all angles. In the case of the 25 PPI material, no tonal peak is observed, which again confirms that the vortex shedding has been effectively eliminated using the porous treatment. The tonal peak for the case of solid trailing edge protrudes by about 25 dB above the broadband energy content while that for porous 80 PPI is in the order of about 18 dB, and almost negligible for porous 25 PPI case at all polar angles. The far-field noise spectra results have shown that the 25 PPI treatment can increase the broadband energy content in the high frequency range *i.e.* up to 8 dB to 10 dB noise increase, which might be due to the frictional forces between the flow and the rough porous surface [6, 38].

One interesting phenomenon discovered in the present study is the generation of a double-peak at the vortex shedding frequency in the case of the solid trailing-edge, as mentioned beforehand. This double peak consists of a dominant peak at $St \approx 0.2$ and a lower amplitude secondary dominant peak at a lower frequency at $St \approx 0.18$. Note that the amplitude of the secondary dominant peak for the solid case is much lower at other angles (θ=45°, 60° and 120°). Moreau and Doolan [39] argued that the existence of multiple dominant peaks in the noise spectra is due to the cellular variation in spanwise vortex shedding frequency, *i.e.* the dominant peak is attributed to the strong regular vortex shedding behind the plate trailing edge, while the secondary dominant peak can be possibly associated with the lower frequency shedding near the plate trailing edge. This, however, requires further experimental and numerical investigations using either 3D time-resolved PIV or high-fidelity Large Eddy Simulation (LES).

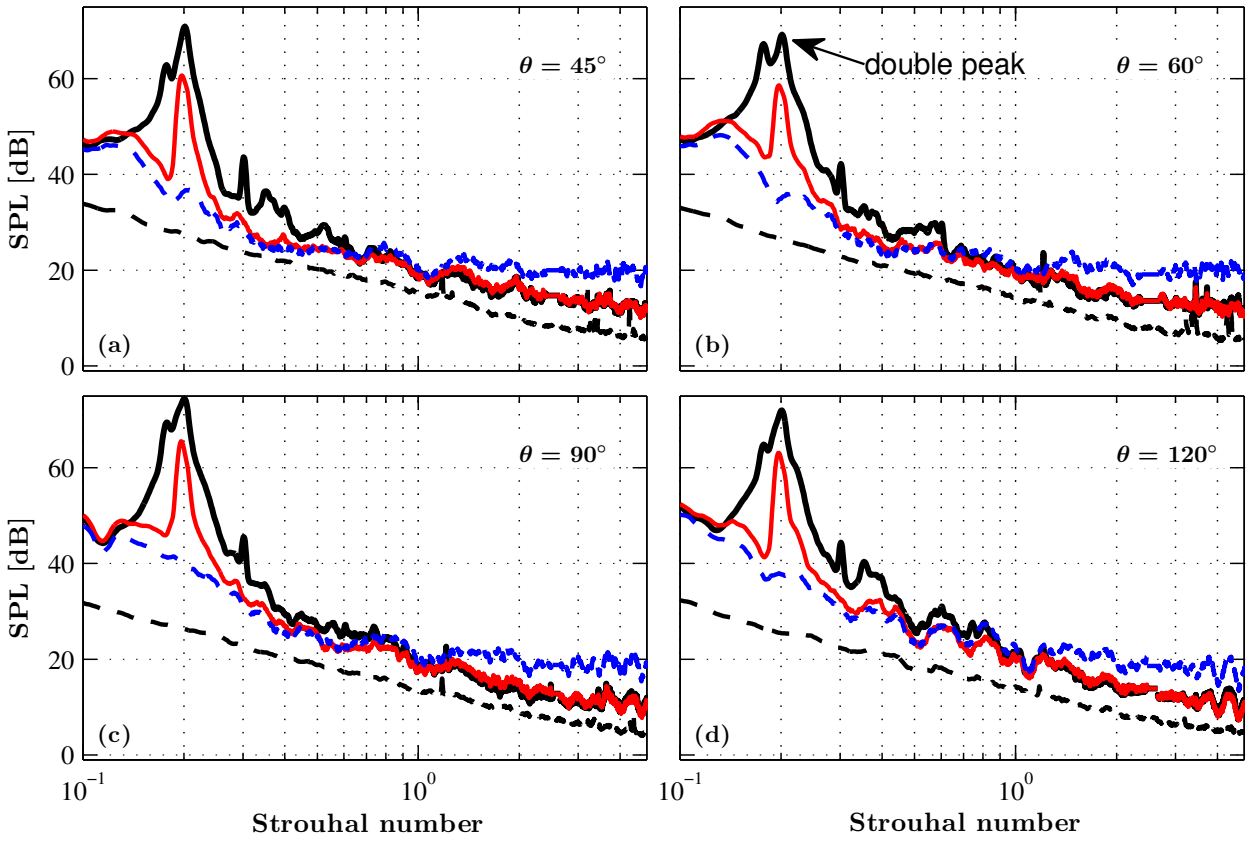

Figure 3: Sound pressure level spectra of the far-field pressure fluctuations with reference to 20μPa at polar angles of θ=45°, 60°, 90° and 120°, measured at U_∞=30 m/s. *Solid trailing edge (——), Porous 80 PPI trailing edge (——), Porous 25 PPI trailing edge (- - -), Background noise (·····).*

Figure 4 presents the contour plot of the far-field sound pressure level at the polar angles of θ=45°, 60°, 90° and 120°, as a function of velocity and frequency with and without the trailing edge porous treatment. The results for the solid case (Fig. 4 (a,d,g,j)) show a clear slope that passes through the Strouhal peaks. These Strouhal peaks correspond to the vortex shedding peak which can be seen for all microphone results, at different polar angles. It can be seen that the sound pressure level at the vortex shedding frequencies is relatively stronger at higher polar angles, especially at the polar angle of 90°, above the plate trailing edge. The vortex shedding peak, however, is not seen at the low velocities ($U_\infty \leq 30\ m/s$). Results also have shown that the first harmonics of the vortex shedding frequency at different velocities can be clearly seen at the polar angles of 45°, 60°, 90° and 120°, with weaker sound pressure level at the vortex shedding peak. In the case of the porous 80 PPI trailing edge, while a weak peak can be observed at the fundamental vortex shedding frequency, the first harmonic ($St = 0.4$ line) of the vortex shedding frequency is suppressed compared to that of the solid case. On the contrary, the 25 PPI material eliminates the vortex shedding peak entirely and an area of high broadband sound pressure level emerges at higher frequencies ($f > 1000$ Hz), which might be due to the frictional forces between the flow and the rough porous surface [6].

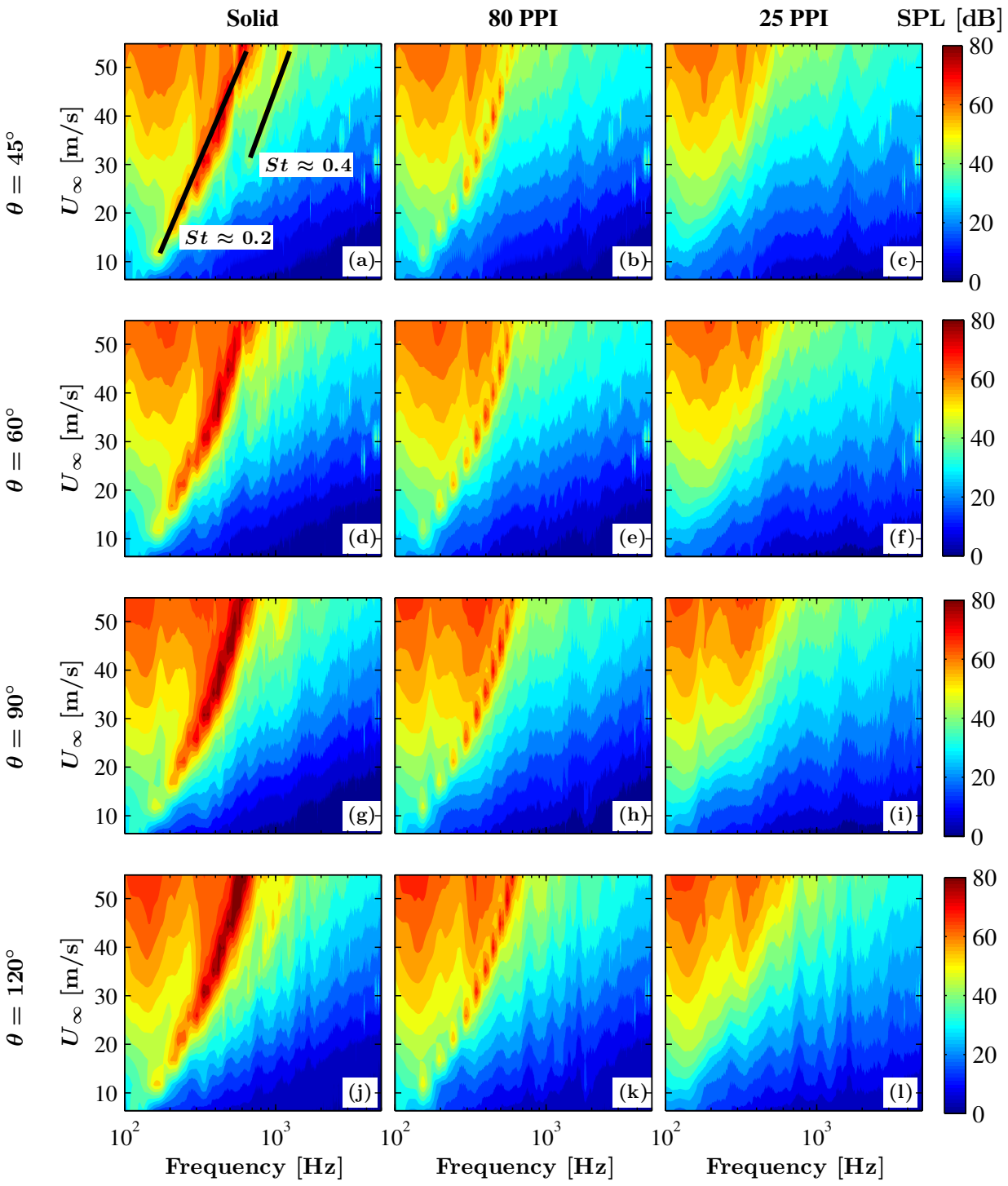

Figure 4: Sound pressure level (SPL [dB]) contour plots of the far-field noise with reference to 20μPa at polar angles of θ=45°, 60°, 90° and 120° as a function of the velocity and frequency.

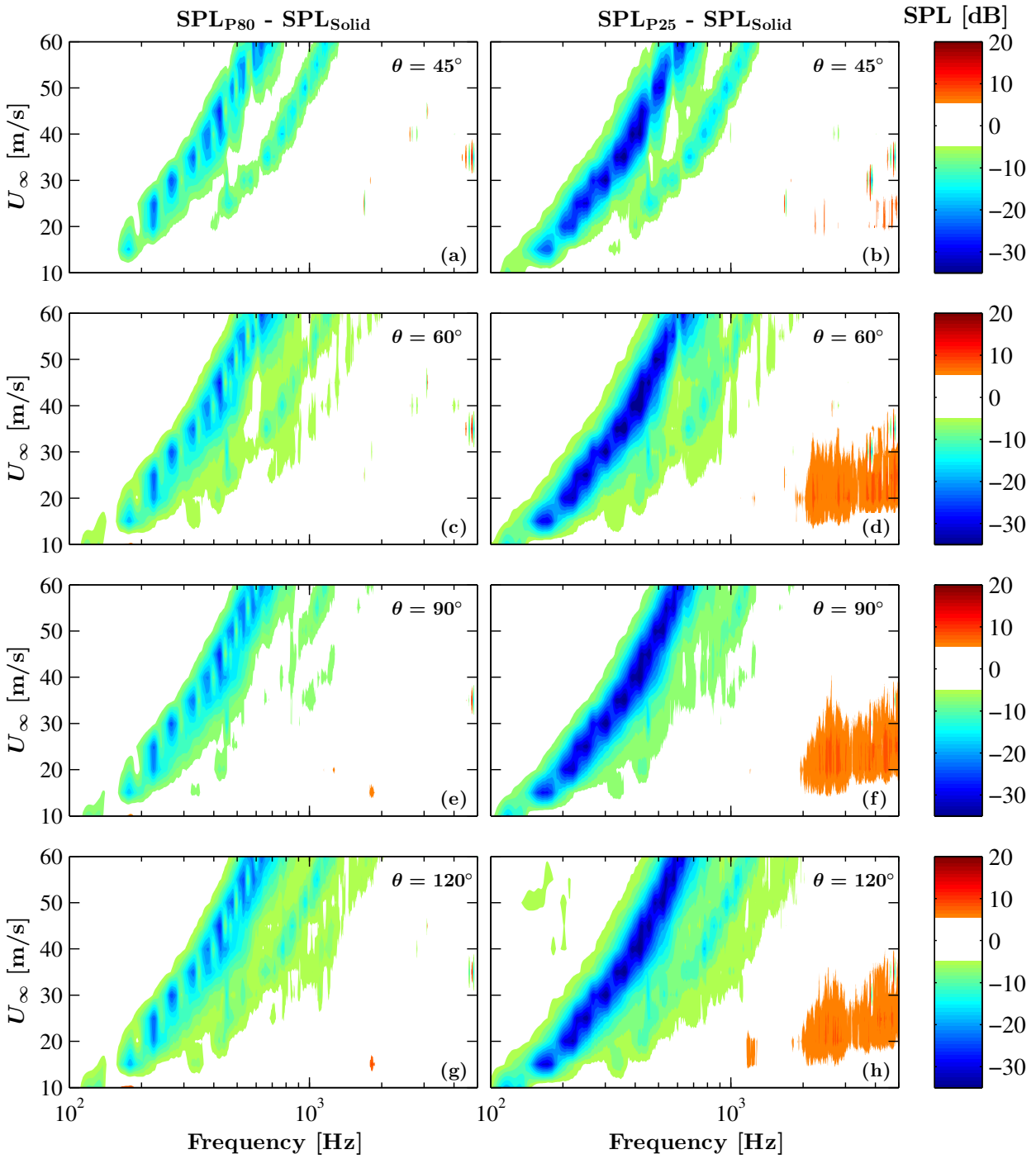

Figure 5: Change in the sound pressure level (ΔSPL [dB]) of the far-field noise with reference to 20μPa at polar angles of θ=45°, 60°, 90° and 120°.

In order to better visualize the far-field noise reduction obtained using porous trailing edge treatments, the changes in the sound pressure level of the far-field noise measured between the solid trailing edge and the 80 PPI and 25 PPI porous trailing edges (ΔSPL = SPL$_{porous}$-SPL$_{solid}$) are presented in Fig. 5. The results in Figs. 5(a) to 5(h) show the contour plots of

ΔSPL as a function of the frequency and the mean velocity at the polar angles of 45°, 60°, 90° and 120°, respectively. As observed in Fig. 4, a clear slope that passes through the Strouhal peaks at the vortex shedding frequency can be seen at different flow velocities. In the case of $\mathrm{SPL}_{80\ \mathrm{PPI}}$-$\mathrm{SPL}_{\mathrm{solid}}$, it can be seen that there is a reduction in the sound pressure level of about 15-20 dB along the $St \approx 0.2$ line at all microphones locations, where vortex shedding is at its most prominent. In the case of $\mathrm{SPL}_{25\ \mathrm{PPI}}$-$\mathrm{SPL}_{\mathrm{solid}}$, a significant vortex shedding tonal noise reduction in excess of about 35 dB is observed at all microphones locations. However, the results have also shown that the porous 25 PPI treatment can increase the broadband energy content of the radiated noise in higher frequency ranges at all the microphones locations. The fundamental and the first harmonic of the vortex shedding frequency can be clearly seen from the results obtained at all the polar angles measured. The noise increase associated with the frictional forces at the surface of plate seems to have a strong dependency on the radiation angle (θ), particularly at low flow speeds ($U_\infty \leq 30\ m/s$).

3.2. Far-field directivity patterns

The directivity plots at different frequencies at the flow speed of U_∞=30 m/s with and without the porous treatments are shown in Fig. 6. The results are presented with different scales for the purpose of better visualization and clarity. At $St = 0.1$, the amplitude of the acoustic waves seems to remain almost similar for all the cases, *i.e.* the porous treatment has no effect on the far-field microphone directivity. At $St = 0.2$, the directivity peaks at $\theta = 90°$ and the lowest directivity can be seen in the downstream microphone location ($\theta = 25°$), for all the trailing edge cases measured. It can be seen that the amplitude of the vortex shedding tone (St=0.2) decreases for the porous treated cases, especially for the 25 PPI case, with up to 35 dB reduction at $\theta = 90°$. The directivity pattern of the radiated sound has a larger number of lobes at St=0.3 and 0.4. It can also be seen that the reduction in the far-field noise for all the treated cases at all the polar angles becomes smaller as the frequencies increases, *i.e.* at higher Strouhal number (St=0.3, 0.4 and 0.5).

A noise increase can be seen in the case of the 25 PPI treatment at St=1.0, 1.5 and 2.0, which might be due to the roughness of the porous surface [38]. This is consistent with the surface roughness results obtained in sub-section§ 2.2.3. In contrast, the directivity of the acoustic waves generated by the lower permeability material (80 PPI) is almost similar to that of the solid case at high frequencies (St=1.0, 1.5 and 2.0), *i.e.* the average roughness value (Ra) is much lower than that of the 25 PPI material, which is consistent with the results obtained in Figs. 3 and 5.

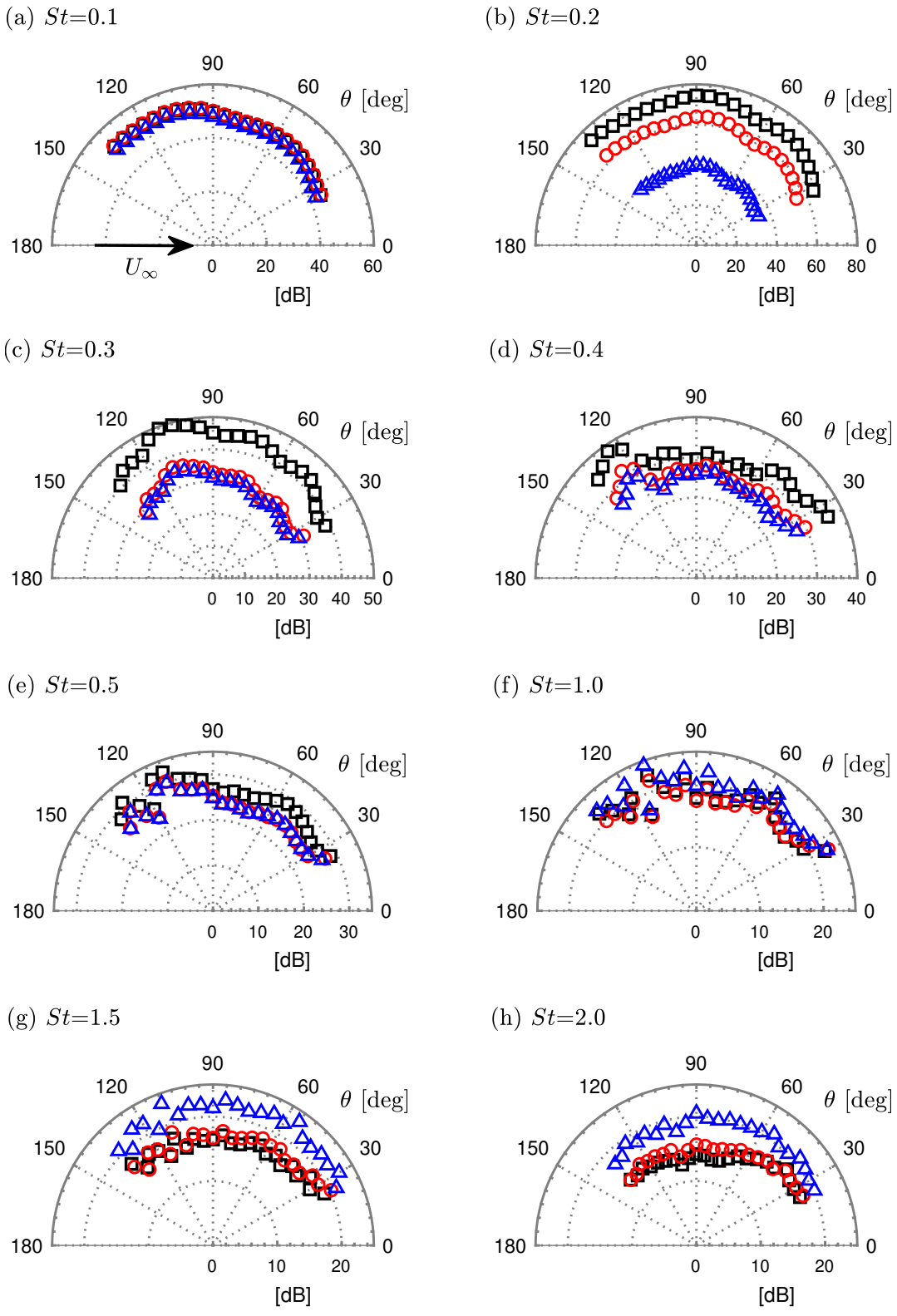

Figure 6: Directivity of the acoustic waves generated by the trailing edge configurations with and without the porous treatments at U_∞=30 m/s for Strouhal number (a) St = 0.1, (b) St = 0.2, (c) St = 0.3, (d) St = 0.4, (e) St = 0.5, (f) St = 1.0, (g) St = 1.5 and (h) St = 2.0. Solid trailing edge □, Porous 80 PPI trailing edge ○ and Porous 25 PPI trailing edge △.

The overall sound pressure level (OASPL) are also obtained by integrating the energy spectrum with respect to frequency. In the present work, the integration is carried out over the frequency f range of 100 Hz to 32 kHz. Figure 7 shows the directivity of the overall sound pressure level for the solid and porous treated cases at U_∞=20 m/s, 30 m/s, 40 m/s and 50 m/s. The results clearly show that the porous trailing edges reduce the overall sound pressure level over the entire polar angle range for all the velocities measured, especially for the 25 PPI material. It can be observed that there is a clear increase in the overall sound pressure level for all the cases with the flow speed. The reduction in the overall sound pressure level varies with the velocities measured. While a significant reduction of the overall sound pressure level of about 25 dB can be seen for the 25 PPI case relative to the solid case at $U_\infty = 20\ m/s$ and $30\ m/s$, a much smaller reduction of the overall sound pressure level is observed for all the porous cases compared to that of the solid case at high velocities ($U_\infty > 30\ m/s$). Note that, at higher velocities, the differences in the OASPL between the two porous cases become insignificant. In the downstream direction $\theta \leq 45°$, the noise reduction by the porous trailing edges are much smaller at all the velocities.

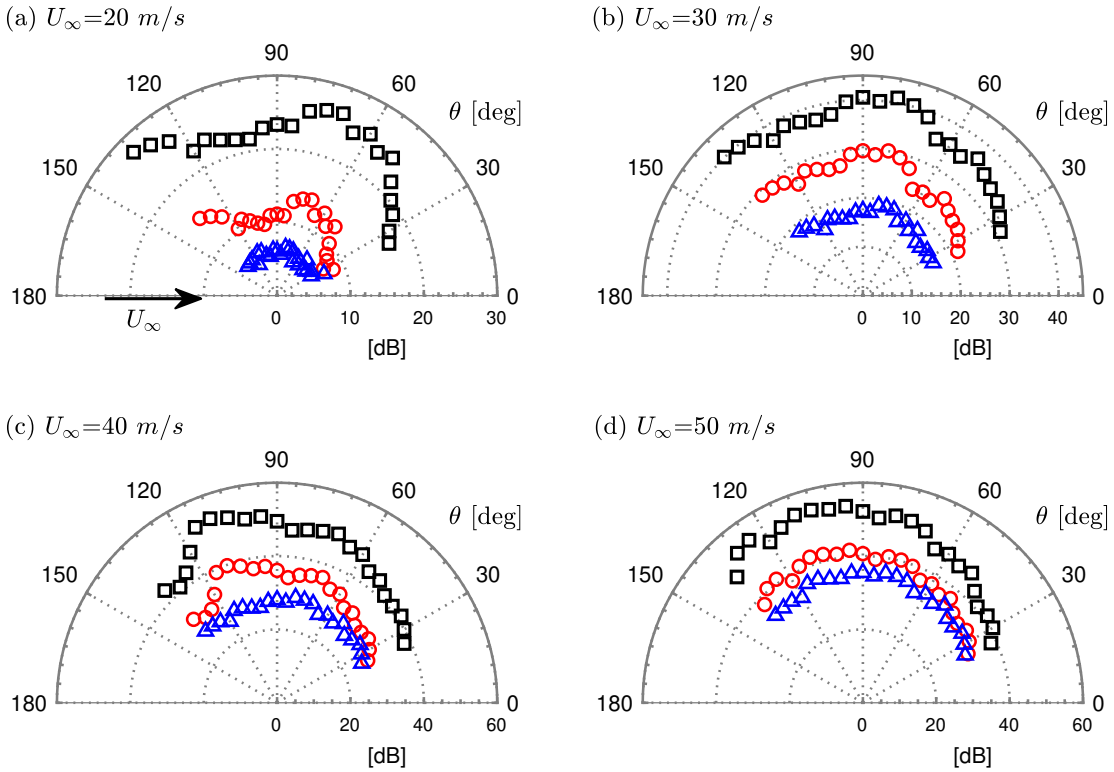

Figure 7: Overall sound pressure level (OASPL) of the acoustic waves generated by the trailing edge configurations with and without the porous treatments at U_∞=20 m/s, 30 m/s, 40 m/s and 50 m/s. Solid trailing edge □, Porous 80 PPI trailing edge ○ and Porous 25 PPI trailing edge △.

3.3. Near-field to far-field analysis

Figure 8 presents the coherence ($\gamma^2_{p'_1 p'_\theta}$) between the surface pressure signals at *p1*, (x/h=-0.35) and the far-field microphone signals at θ = 45°, 60°, 90° and 120° at the free-stream

velocity of U_∞=30 m/s. The *p1* surface pressure transducer location corresponds to the main region where strong flow acceleration occurs. The flow acceleration at the trailing edge was previously discussed in another paper [6]. The coherence between the surface pressure and the far-field pressure signals can be found from,

$$\gamma^2_{p'_1 p'_\theta}(f) = \frac{|\Phi(f, p'_1, p'_\theta)|^2}{|\Phi(f, p'_1, p'_1)||\Phi(f, p'_\theta, p'_\theta)|}, \tag{1}$$

where $\Phi(f, p'_1, p'_\theta)$ denotes the cross-power spectral density function between the surface pressure (p'_1) and the far-field pressure signals (p'_θ) at different polar angles.

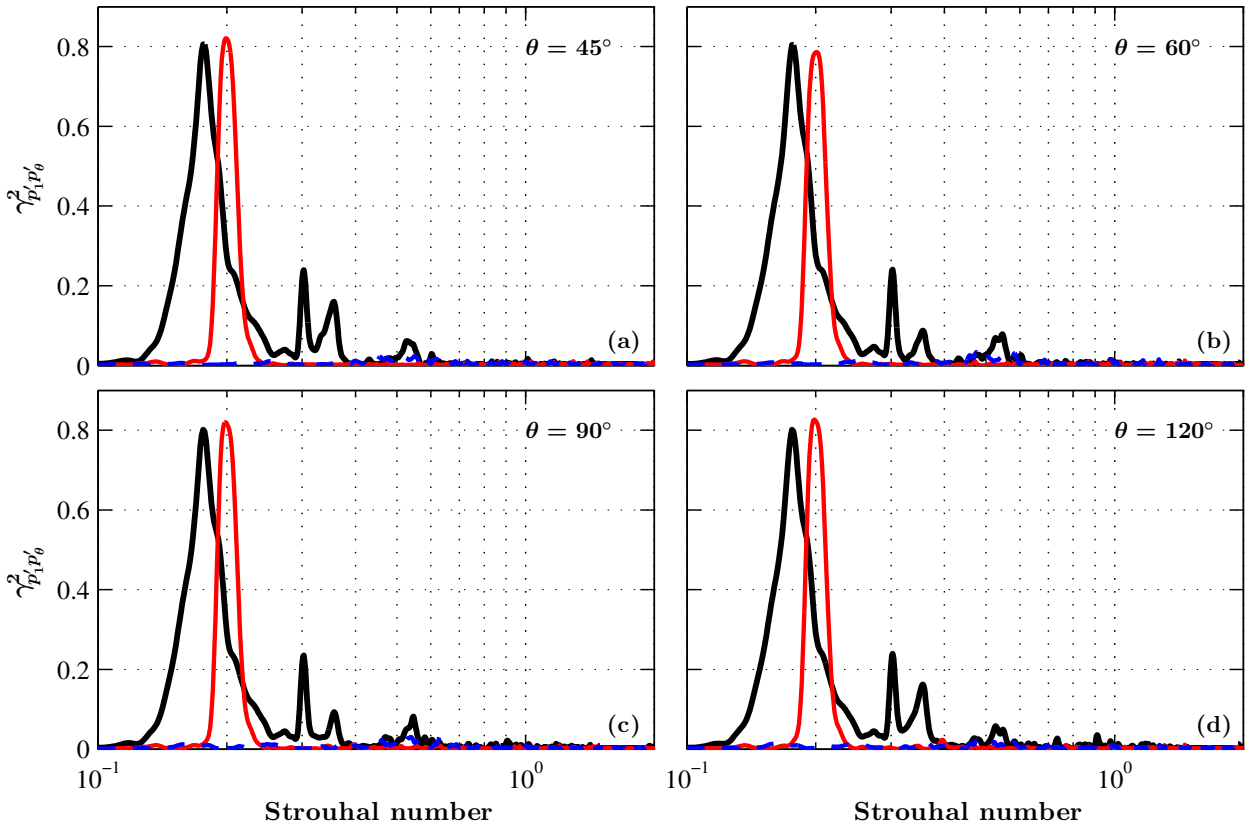

Figure 8: Near-field to far-field coherence between a surface pressure transducer at $x/h = -0.35$ (*p1*) and far-field microphones at $\theta = 45°$, $\theta = 60°$, $\theta = 90°$ and $\theta = 120°$. The measurements are taken at U_∞=30 m/s.*Solid trailing edge (—), Porous 80 PPI trailing edge (—), Porous 25 PPI trailing edge (- - -).*

The coherence ($\gamma^2_{p'_1 p'_\theta}$) results are plotted as a function of the Strouhal number ($St = fh/U_\infty$). In the case of the solid trailing edge, as expected, a strong coherence can be observed at the vortex shedding frequency, about St =0.18 between the pressure signals at all the polar angles measured. The fundamental, first and second harmonics of the coherence ($\gamma^2_{p'_1 p'_\theta}$) at the vortex shedding frequency can also be clearly seen from the results of the solid trailing edge. The $\gamma^2_{p'_1 p'_\theta}$ results for the solid trailing edge seem to only occur at the lower amplitude secondary dominant peak at St =0.18 observed in the sound pressure level spectra in the far-field region (see Fig. 3). In the case of porous 80 PPI trailing edge, it can

be observed that the fundamental frequency has a very tonal behaviour with no broadband content and that the treatment is able to eliminate the harmonics seen in the case of the solid trailing edge. On the contrary, the 25 PPI material eliminates the vortex shedding peak entirely and exhibits an almost zero-coherence level over the whole frequency range, indicating that the two pressure signals are completely uncorrelated.

4. Flow-field analysis

The results in Sec. 3 have shown that the porous treatments can alter the far-field noise signature of the blunt trailing edge. In the following section, we will further investigate the flow field and the turbulent kinetic energy of the boundary layer and wake flow field. The production and dissipation rate of the turbulent kinetic energy will also be studied. Moreover, a comprehensive study on the relationship between the trailing edge surface pressure field and the flow turbulence structures responsible for the pressure exerted on the wall have also been carried out.

4.1. Boundary layer analysis

The normalized time-averaged mean and root-mean-square (rms) boundary layer velocity profiles are shown in Fig. 10. The schematic of the plate trailing edge and the position of the hot-wire for the boundary layer (BL_{1-3}) measurements are presented in Fig. 9. The boundary layer measurements were carried out using a single hot-wire probe at the free-stream velocity of $U_\infty = 20\ m/s$, corresponding to the Reynolds number of $Re_h = 2.6 \times 10^4$. The measurements were taken over the whole trailing edge section area ($x/h = -0.35$ and -1.90) and at the region upstream ($x/h = -2.60$) of the trailing edge section. The data were collected with a fine spatial resolution between $y^{'}/h \approx 0$ and $y^{'}/h \approx 2.5$, above the plate. Since the fluid velocity approaches zero at the solid boundary (*i.e.* no-slip condition), the $y^{'}$-axis was normalized by the boundary layer thickness BL_1 over the solid surface immediately upstream of the porous treatment. The no-slip boundary condition does not hold over the porous surface since the fluid can penetrate and sink into the porous medium [40].

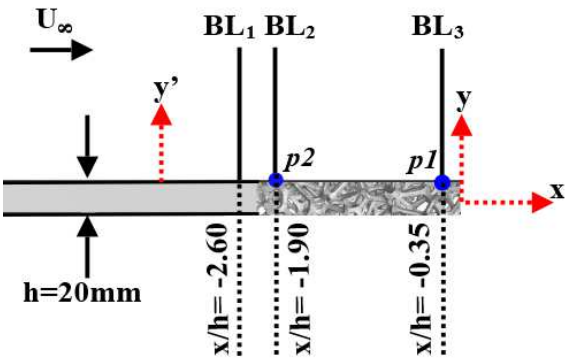

Figure 9: Schematic of the flat plate and the position of the hot-wire for boundary layer (BL_i) measurements.

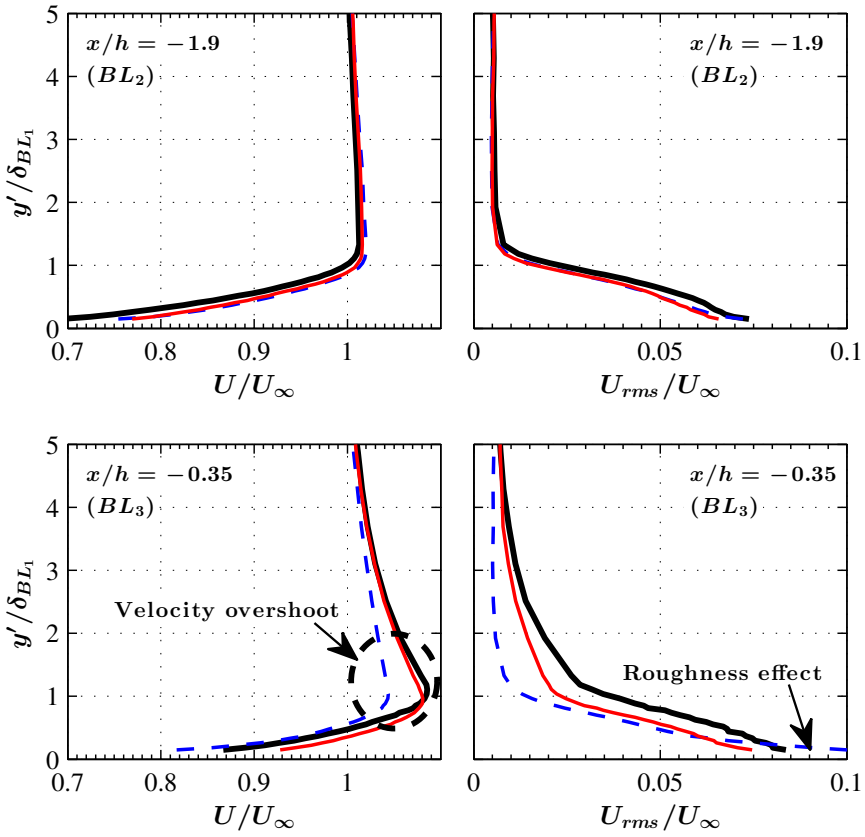

Figure 10: Boundary layer mean (U/U_∞) and rms (U_{rms}/U_∞) velocity profiles at $x/h = -1.9$ and $x/h = -0.35$ over the blunt trailing-edge. *Solid trailing-edge (——), Porous 80 PPI trailing-edge (——), Porous 25 PPI trailing-edge (- - -).*

The mean and rms velocity profiles upstream of the trailing edge section (BL_1) are found to be similar for all the cases and are therefore not presented here. Results have shown that the boundary velocity profile for all the solid and treated cases drastically deviate from the standard turbulent boundary layer form by moving toward the trailing edge, due to the plate bluntness effects. In the case of the solid trailing edge, at the downstream location (BL_3), the results clearly show the peak of the velocity overshoot, which occurs at $y^{'}/BL_1 = 1$, implying the emergence of flow acceleration at the trailing-edge region. The rms velocity results for the solid case show a higher level of energy content (*i.e.* velocity fluctuations) in the boundary layer region, compared to that of the porous cases. The boundary layer mean velocity profiles in the case of the 80 PPI trailing edge are found to be very similar to the solid case, with a little reduction in the velocity overshoot at BL_3. The results have shown that the 80 PPI material is able to reduce the rms velocity fluctuations over the whole boundary layer region compare to the solid case. The results for the 25 PPI treated trailing edge, on the other hand, shows that the velocity overshoot can be significantly suppressed. The rms velocity results for the 25 PPI material clearly show that the whole energy cascade of the boundary layer changes greatly, particularly over the outer layer part of the boundary layer region. However, the flow-field in the case of the 25 PPI material also experiences an increase in the rms velocity fluctuations at the near the wall region at BL_3, which is attributed to the frictional forces due to the effect of the material rough surface. This is in agreement with

the surface roughness results obtained in sub-subsection§ 2.2.3. Note that, although there is a slight increase in the velocity fluctuations over the small region of the boundary layer profile at the vicinity of the 25 PPI surface, the overall energy content in the outer layer regions, concerning the low frequency aspect of the noise generation from the large coherent structures can be significantly reduced.

4.2. Wake flow analysis

To better understand the role of porous treatments in the modification of the vortex formation region and vortex shedding, PIV measurements were conducted at the flow velocity of $U_\infty = 20\ m/s$. Figure 11 shows the time-averaged streamwise velocity measured along the wake centerline (y/h=0). The vortex formation length is presented as a function of the wake distance (x/h). The square markers overlaid on the velocity curves indicate the non-dimensionalized vortex formation length (L_f/h) of each case. According to Bearman [41], the L_f/h is the point where the maximum streamwise velocity fluctuations is obtained along the wake centerline, *i.e.* the end of the vortex region. This indicates that the end of the vortex region formation coincides with the location at which the flow field from outside the wake crosses the axis. The contour maps of the time-averaged normalized velocity of the vortical structures behind the blunt plate are also embedded in Fig. 11.

The results show that the velocity deficit in the case of the solid trailing edge is about U/U_∞=-0.27 at $x/h \approx 0.5$, while in the case of the 80 PPI and 25 PPI material, a much lower velocity deficit is observed at about U/U_∞=-0.2 and -0.04, respectively. The position where the velocity minimum (dip) occurs moves downstream, from $x/h \approx 0.75$ for the 80 PPI material to $x/h \approx 1.1$ for the 25 PPI material. The velocity at the wake centerline for all the cases converge to the same velocity further downstream in the fully turbulence developed region at $x/h > 4$. As can be observed, the solid trailing edge exhibits the shortest L_f/h, with a pair of symmetrical counter-rotating vortices close to the plate trailing edge. With the implementation of the 80 PPI treatment, the L_f/h mildly increases compared to the solid case, with a slight shift in the vortex structures from the trailing edge. The application of the 25 PPI treatment causes the vortex formation length to progressively increase, moving further downstream of the trailing edge with significant changes to the vortex structures. The recirculation region and the L_f/h locations of the solid and porous cases are provided in Table 1. The results here imply that a significant delay in the recirculation region, *i.e.* vortex shedding, can be achieved using highly permeable materials (porous 25 PPI). In the present analysis a special emphasis has been placed on the understanding of the presence of an acceleration region near the trailing edge, as a result of the pressure difference at the trailing edge, see Fig. 11. The emergence of the flow acceleration can also be related to the development of the re-circulation region and the vortex core and significant variation in the pressure field over the surface of the blunt trailing edge. The flow is accelerated near the trailing edge area due to the pressure difference inside and outside the vortex core in the near-wake region of the plate. The flow-field results for the solid case clearly show the emergence of a strong acceleration of the streamwise velocity and velocity overshoot near the trailing edge, which is consistent with the boundary layer results observed in Fig. 9. While the 80 PPI material exhibits a much broader flow acceleration zone compared to the solid case, the 25 PPI material shows a much lower flow acceleration and velocity overshoot in the trailing edge region. The emergence of a broader acceleration region and the difference in the

intensity of the acceleration region in the case of the porous trailing edge can be potentially due to the flow-porous permeability effect [7]. The results observed from the 80 PPI material are almost identical to that of the solid case, which demonstrate that, in order to enable flow-penetration into the porous medium, a longer flow and porous surface interaction is needed [6]. The changes observed in the case of the 25 PPI material are due to several potential factors, such as the flow penetration into the porous medium, hydrodynamic absorption and the existence of a quasi-periodic recirculating flow field inside the porous medium. A thorough study of the emergence of the hydrodynamic field and quasi-periodic structure inside the porous medium was previously reported in [6].

Figure 12 shows the normalized streamwise ($\overline{u'u'}/U_\infty^2$) and wall-normal ($\overline{v'v'}/U_\infty^2$) Reynolds stress terms measured along the wake centerline. The square markers overlaid on the $\overline{u'u'}$ results (Fig. 12(a)) indicate the non-dimensionalized vortex formation length (L_f/h), which is consistent with the results obtained in Fig. 11. Interestingly, in the case of the solid trailing edge, the $\overline{u'u'}$ stress term exhibits two distinct peaks at $x/h \approx 0.3$ and $x/h \approx 1.04$. The $\overline{u'u'}$ peak at $x/h \approx 0.3$ occurs just upstream of the location of the wake recirculation closure ($x/h \approx 1.04$). This profile is similar to that observed by Norberg [42] and Lehmkuhl *et al.* [43], based on their measurements for a circular cylinder. On the contrary, the $\overline{u'u'}/U_\infty^2$ along the wake centerline for the porous cases is rather different, with only one peak at the vortex formation length (L_f/h). A lower level of fluctuations can be seen in the case of porous trailing edges, suggesting that the flow structures are less energetic and turbulent than the solid trailing edge. The $\overline{v'v'}$ distributions are shown in Fig. 12(b). The notable feature here is that the level of $\overline{v'v'}$ term is twice, or more, larger than that of the $\overline{u'u'}$ term along the wake centerline for all the trailing edge configurations. Bevilaqua [44] indicated that the increase in the v' fluctuations is associated with the vortex shedding formation, with the presence of a highly anisotropic flow at this region. The anisotropy level related to the vortex formation region was briefly discussed in the previous studies [6]. In the case of the solid trailing edge, the $\overline{v'v'}$ stress term increases in the near wake region, peaks at the vortex formation length region and quickly decays after $x/h \gtrsim 1.04$. In the case of the 80 PPI trailing edge, while a slight reduction of the $\overline{v'v'}$ stress term can be seen in the near wake ($x/h \lesssim 0.7$), the magnitude of the $\overline{v'v'}$ has slightly increased at the vortex formation region compared to the solid trailing edge case and slowly decays after $x/h \gtrsim 1.1$. As anticipated, the $\overline{v'v'}$ stress term is the lowest for the 25 PPI material along the wake centerline and mildly increases at the downstream locations ($x/h \gtrsim 3.7$). It can also be seen that there is a significant reduction at the peak location ($x/h \approx 2.5$) of the $\overline{v'v'}$ stress term compared to that of the solid and porous 80 PPI cases. The peak of the $\overline{v'v'}$ is seen to move further downstream, where a weak vortex recirculation region is expected (see Fig. 11), followed by a much slower decay of the $\overline{v'v'}$ after $x/h \gtrsim 2.5$.

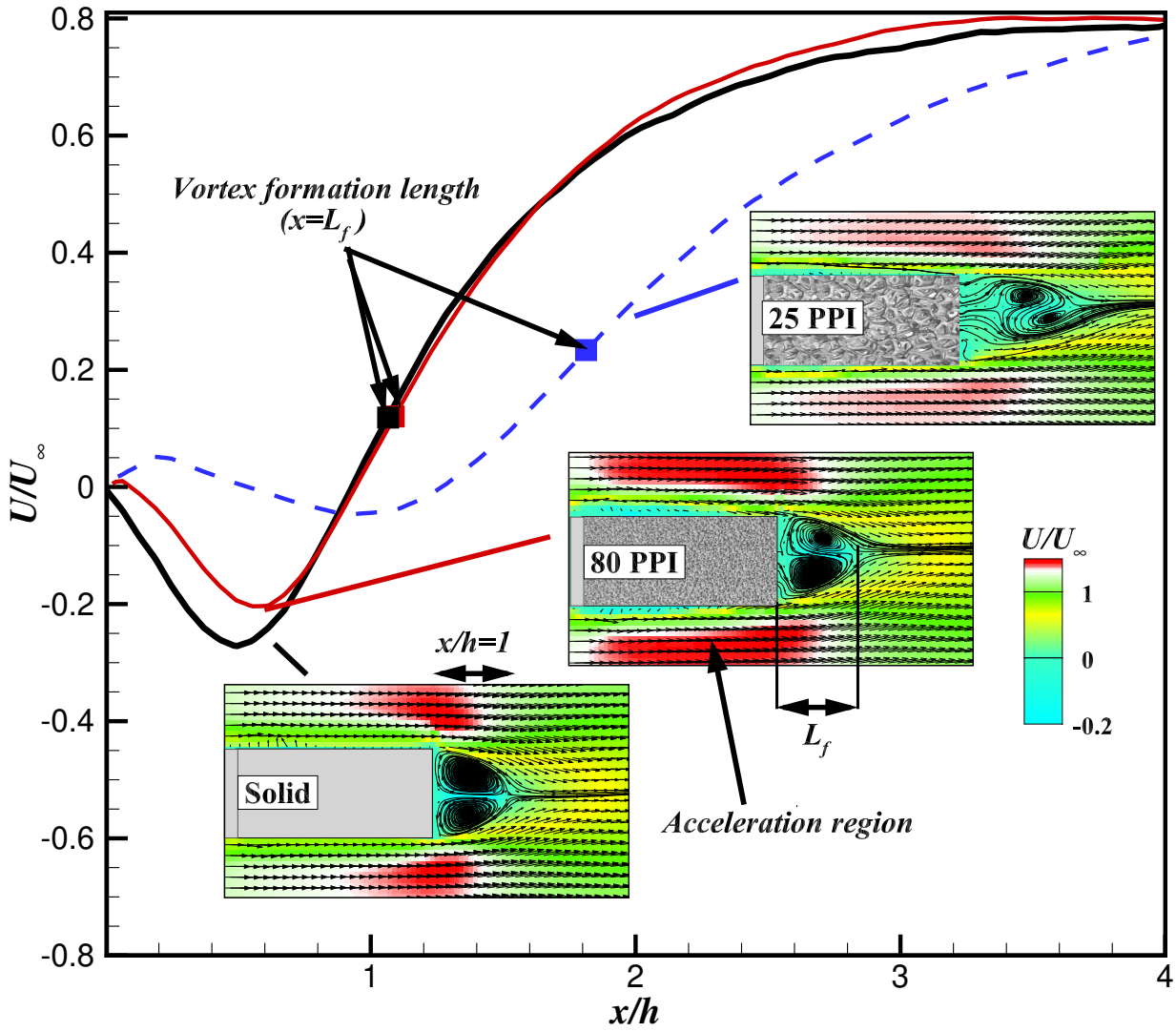

Figure 11: Effects of the recirculation in the wake formation and development: time-averaged streamwise velocity measured along the wake centerline (y/h=0), and time-averaged normalized velocity components of the vortical structures behind the blunt plate. The square symbols overlaid on the streamwise velocity results line correspond to the vortex formation length (L_f/h). *Solid trailing-edge (—), Porous 80 PPI trailing-edge (—), Porous 25 PPI trailing-edge (- - -).*

Table 1: The recirculation region and the vortex formation length (L_f/h) locations for the solid and porous cases.

Cases	**Recirculation zone**	**Vortex formation length (L_f/h)**
Solid	$0.05 \lesssim x/h \lesssim 1.04$	1.04
Porous 80 PPI	$0.15 \lesssim x/h \lesssim 1.1$	1.1
Porous 25 PPI	$0.5 \lesssim x/h \lesssim 1.9$	1.9

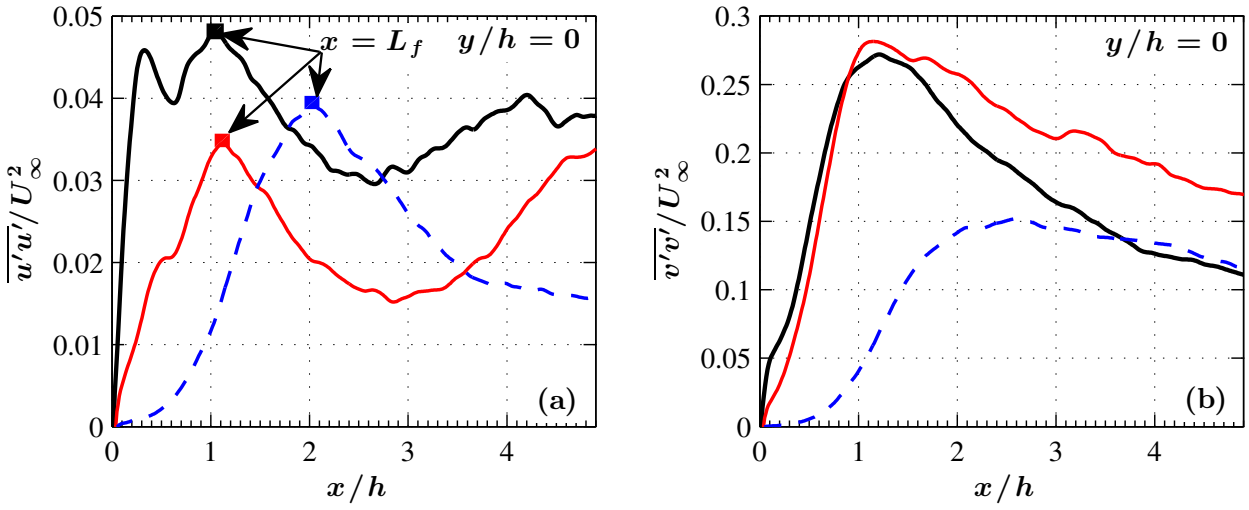

Figure 12: Effects of the recirculation in the wake formation and development: averaged $\overline{u'u'}/U_\infty^2$ and $\overline{v'v'}/U_\infty^2$ fluctuations along the wake centerline. *Solid trailing-edge (—), Porous 80 PPI trailing-edge (—), Porous 25 PPI trailing-edge (- - -).*

4.2.1. TKE production and dissipation in the wake region

In addition to the Reynolds stress terms ($\overline{u'u'}$ and $\overline{v'v'}$) shown in Fig. 12, to better understand the nature of the wake flow, the spatial variation of the turbulent production and dissipation rates has been studied using the two-dimensional PIV results over the x-y plane. A standard form of the turbulent kinetic energy (TKE) transport equation is given by Hinze [45]. Given the two-dimensional nature of the wake flow in the present study, one can reasonably assume that $\overline{U_3}$=0 and $\partial u_3'/\partial x_3$=0. In such a case, the TKE production rate (P_k) and dissipation rate (ϵ_k) can be found from,

$$P_k = -(\overline{u'^2} - \overline{v'^2})\frac{\partial U}{\partial x_1} - \overline{u'v'}\left(\frac{\partial U}{\partial x_2} + \frac{\partial V}{\partial x_1}\right), \tag{2}$$

$$\epsilon_k = -\upsilon\left[\overline{\left(\frac{\partial u'}{\partial x_1}\right)^2} + \overline{\left(\frac{\partial u'}{\partial x_2}\right)^2} + \overline{\left(\frac{\partial v'}{\partial x_1}\right)^2} + \overline{\left(\frac{\partial v'}{\partial x_2}\right)^2}\right], \tag{3}$$

where x_1, x_2 and x_3 are the streamwise, wall-normal and spanwise spatial coordinates, respectively and the mean velocity components are denoted by U and V.

The production and dissipation field contour plots over a large wake domain of $0 < x/h < 3$ and $|y/h| < 1.5$ are shown in Fig. 13. In the case of the solid trailing edge, the results reveal that there is strong TKE production in the wake recirculation region close to the trailing edge, where the maximum reverse flow is observed (see Fig. 11) due to the presence of vortex shedding. This supports the maximum Reynolds stresses results observed in [6]. The dissipation intensity behind the solid trailing edge peaks at the tips of the plate ($y = \pm 0.5h$) and is particularly large within the shear layers and the region where the maximum reverse flow is seen. The turbulence dissipation, however, is less strong at the far-wake region (recovery zone). In the case of the 80 PPI material, the region of maximum turbulence production is delayed slightly to further downstream locations, with a shift in the

vortex structures from the trailing edge, as observed in Fig. 11. The dissipation intensity, on the other hand, shows that there is an area of minimum dissipation in the near wake region, where the vortex shedding is absent. Similar to the results observed in the case of the solid trailing edge, the TKE dissipation is found to be much stronger at the recirculation region ($0.15 \lesssim x/h \lesssim 1.1$).

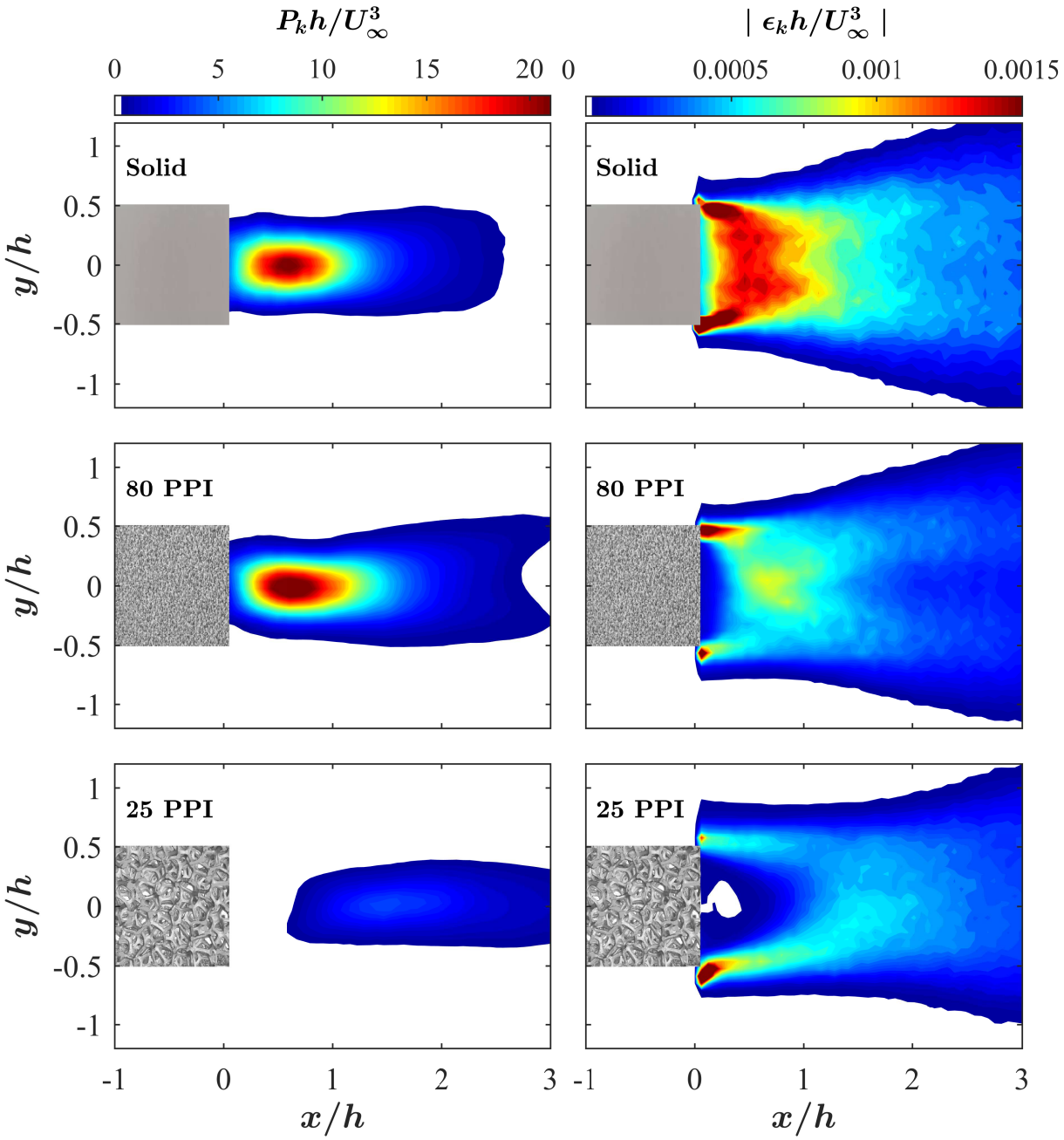

Figure 13: Contours of the turbulent statistical quantities, normalized production (a,b,c) and normalized dissipation (d,e,f).

In the case of the 25 PPI material, the turbulence production gets completely attenuated or become negligible in the near wake region, *i.e.* no presence of vortex shedding and the production peak moves to further downstream locations where the recirculation region is observed (see Fig. 11). The TKE production in the case of the porous 25 PPI is lower than the solid and 80 PPI tailing edge cases. Furthermore, the dissipation is minimum near the trailing edge and gradually increases at the downstream locations, where the presence of a weak vortex shedding structures is observed (see Fig. 11). In the case of the 25 PPI trailing edge, the turbulence dissipation becomes negligible in the vicinity of the trailing edge ($0 \leq x/h \leq 0.5$), particularly at the centerline of the trailing edge ($y/h = 0$). Moreover, a much lower dissipation intensity is seen, which is confined within an arc, stretches downstream to the area where the weak recirculation has previously been observed in Fig 11. The results here generally show that the turbulence production and dissipation behind the trailing edge are related to the formation of vortex shedding behind the trailing edge.

4.2.2. Wake spectral and velocity-pressure coherence analysis

The turbulent structures properties within the wake region have been studied using the energy-frequency content of the total wake velocity PSD (ϕ_{uu}+ϕ_{vv}). Figure 14 shows the results of the total power spectral density (PSD) of the wake velocity as a function of the Strouhal number at several locations downstream of the cylinder ($x/h = 1$ and 2), along the trailing edge lip-line ($y/h = 0.5$) and the centreline ($y/h = 0$). The measurement locations were chosen based on the expected location of the vortex formation region (see Fig. 11), *i.e.* where the maximum streamwise velocity fluctuations is obtained along the wake centerline. In the case of the solid trailing edge, the fundamental and the first harmonic tones of the vortex shedding can be clearly seen at the wake shear layer ($x/h = 1$ and 2), due to the presence of vortex shedding, as shown in Fig. 11. The finding also supports the maximum TKE production and dissipation intensity in the wake observed in Fig. 13. The fundamental tone, however, disappears at the wake centerline ($y/h = 0$) while the first and second harmonics of the vortex shedding can be clearly seen outside of the vortex formation region, $x/h = 2$. A similar trend of the solid case can be seen in the case of the 80 PPI porous material, with the fundamental peak of the total wake velocity PSD is slightly shifted to higher St numbers, due to the shift in the vortex formation region, as seen in Fig. 11. In the case of the 25 PPI porous material, no tonal peak is observed in the near wake region ($x/h = 1$), due to the increase in the vortex formation length (L_f/h), as shown in Fig. 11, leading to the reduction of the turbulent velocity fluctuations in this region. The results also show that in the case of the 25 PPI material, the vortex structures gain more energy at $x/h = 2$, where the fundamental and first harmonics can be seen again, indicating the emergence of a delayed vortex shedding, as previously shown in Fig. 11. The fundamental tonal peak protrudes by about 8 dB above the broadband energy content for the solid and 80 PPI case while in the case of the first harmonic, it can be seen that the 80 PPI material can result in a sharper and stronger tone than the solid case. The tonal peak in the case of the 25 PPI material, however, protrudes only a few dB above the broadband energy content, much smaller compared to the solid and 80 PPI cases. The results also show clearly that the porous treatments can significantly reduce the broadband energy content of the velocity PSD over the whole frequency region compared to that of the solid case.

In order to better understand the characteristics of the wake turbulent structures and

their relationship with the pressure field exerted on the surface, coherence studies between the streamwise velocity in the wake and the surface pressure transducer signals at $p1$, *i.e.* main region where strong flow acceleration occurs, have been carried out. Figure 15 shows the coherence between the surface pressure fluctuations at $p1$ and the streamwise velocity in the wake shear layer ($y/h = 0.5$) measured downstream of the solid and porous trailing edges ($0.1 \leqslant x/h \leqslant 10.45$). The velocity-pressure coherence ($\gamma^2_{u_i'p'}$) results are plotted as a function of the Strouhal number. In the case of the solid trailing edge, a strong coherence can be observed at the fundamental shedding frequency, about $St \approx 0.2$ over the entire wake region ($0.1 \leqslant x/h \leqslant 10.45$), particularly in the near wake area. The velocity-pressure coherence,$\gamma^2_{u_i'p'}$, shows a tonal behaviour but also with a strong broadband characteristic at around the fundamental tone. In the case of the 80 PPI treatment, a similar strong coherence level can be observed at the vortex shedding frequency, but with a narrower frequency width compared to that of the solid case. A similar behaviour was observed in Fig. 3, where the 80 PPI is showing much narrower tonal peak compared to the solid case, indicating the lack of presence of three-dimensional structures in the case of the 80 PPI porous material. In the case of the 25 PPI material, a much weaker coherence profile can be seen at the vortex shedding frequency over the entire wake shear layer region. A stronger coherence intensity can be seen at around ($2 \leqslant x/h \leqslant 4$), which is consistent with the small peaks observed in Fig. 15 due to the presence of a delayed vortex shedding region as seen in Fig. 11.

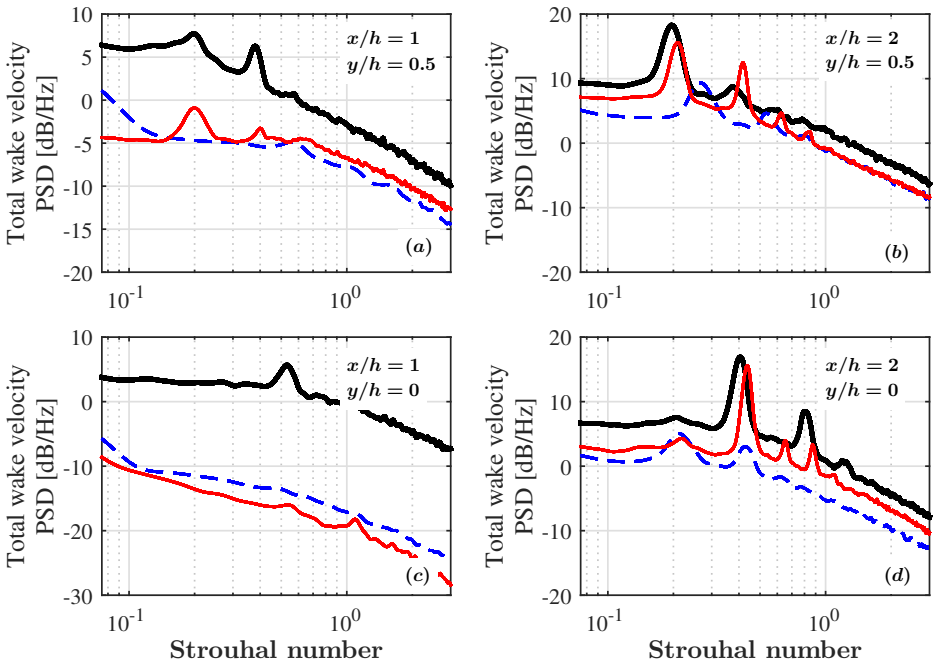

Figure 14: The energy-frequency content of the total wake velocity PSD (ϕ_{uu}+ϕ_{vv}) in the wake region. *Solid trailing edge (—), Porous 80 PPI trailing edge (—), Porous 25 PPI trailing edge (- - -).*

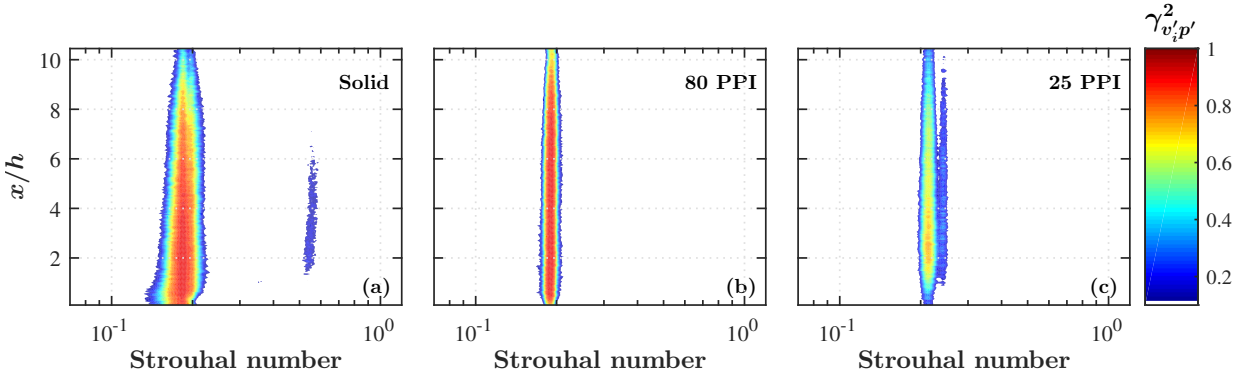

Figure 15: Velocity-pressure coherence, $\gamma^2_{u'_i p'}$ at different streamwise locations in the wake shear layer.

4.2.3. Boundary layer velocity-pressure correlation analysis

In characterizing the noise generated from the trailing edge, it is essential to examine both the flow-field and the pressure exerted on the surface. The correlation studies between the surface pressure fluctuations and the velocity field within the boundary layer were conducted in order to identify the characteristics of the boundary layer turbulent structures and their role on the pressure field exerted on the surface. Simultaneous boundary layer flow and surface pressure measurements were performed at two locations upstream of the trailing edge (see Fig. 2), namely *p1* and *p2*, for the flow velocity of 20 m/s. A cross-wire probe was used and the data had been collected between $y' \approx 0$ mm and 50 mm at 49 locations above each transducer. Figure 16 presents the velocity-pressure correlation ($R_{u'p'}$ and $R_{v'p'}$) results within the boundary layer at different distances from the trailing edge. The space-time correlation between the velocity and the surface pressure fluctuations can be obtained from,

$$R_{u'_i p'}(\xi_{y'}, \tau) = \frac{\overline{u'_i(x, \xi_{y'}, t+\tau) p'(x, 0, t)}}{u'_{i_{rms}} p'_{rms}}, \tag{4}$$

where p' is the wall pressure fluctuations, u'_i corresponds to the u' and v' fluctuating velocities in the streamwise and vertical directions, τ denotes the time-delay between the pressure signals and $\xi_{y'}$ is the separation distance between the boundary layer velocity measurement locations normal to the pressure transducer at the plate surface (y'). The y-axis of the velocity-pressure correlation plots have been normalized by the boundary layer thickness at BL_1. Equation 4 reduces to the two-point correlation function ($R_{u'_i p'}(\xi_{y'})$) when $\xi_{y'} = 0$.

Figure 16 presents the correlation between the streamwise (u') and wall-normal (v') velocities and the surface pressure fluctuations at different axial locations for the solid and porous trailing edges. In the case of the solid trailing edge, at the upstream location p_6 (x/h= -1.9), where the flow acceleration is absent, an overall negative streamwise-pressure correlation ($R_{u'p'}$) can be observed, which peaks at about the location of the flow velocity overshoot ($y'/\delta_{BL_1} = 1$). Moving closer to the trailing edge (p_1, x/h= -0.35), where the flow experiences strong acceleration, a much stronger positive $R_{u'p'}$ correlation can be observed. In the case of the pressure and vertical velocity correlation ($R_{v'p'}$), a small negative correlation can be seen for the locations upstream of the trailing edge locations (x/h= -1.9, -1.3). In the

vicinity of the trailing edge (x/h= -0.35), the $R_{v'p'}$ correlation increases, with its peak at the boundary layer velocity overshoot point ($y'/\delta_{BL_1} = 1$). The $R_{v'p'}$ results also show a negative correlation in the near wall region ($y'/\delta_{BL_1} \lesssim 1$) and positive correlation above the overshoot region. The increase in the correlation value in the trailing edge area can be attributed to the flow acceleration and strong contribution of the vertical flow velocity component to the exerted surface pressure, which is also in agreement with the observations made earlier in Fig. 10 at x/h=-0.35. In the case of a flat plate fitted with a porous 80 PPI trailing edge, for locations immediately after the solid part (x/h= -1.9), the $u' - p'$ and $v' - p'$ correlations reduce to nearly zero, indicating no communication between the boundary layer structures and the surface pressure. However, at the further downstream locations, the porous 80 PPI trailing edge behaves very similar to that of the solid case for both of the $R_{u'p'}$ and $R_{v'p'}$ components.

The correlation results obtained for the porous 25 PPI trailing edge has shown some very interesting features. Results have shown that, in general, the use of a highly permeable surface significantly reduces both the $R_{u'p'}$ and $R_{v'p'}$ correlations compared to the solid and porous 80 PPI trailing edge cases. More importantly, the contribution from the velocity overshoot region has completely vanished, which is consistent with the results presented in Fig. 10. For both the $R_{u'p'}$ and $R_{v'p'}$ components, the correlation over the entire boundary layer region for the porous 25 PPI treatment always remains negative, but it increases in amplitude for locations near the trailing edge. Another interesting observation is that the $R_{u'p'}$ correlation in the near the wall region ($y'/h \lesssim 0$), dominated by surface frictional forces, as seen previously in Figs. 3 and 4, is nearly zero. However, the correlation peak value increases to almost $R_{u'p'} \approx$ -0.2 at about $\xi_{y'}/\delta_{BL_1} \lesssim 1$, which might be associated with the large turbulent structures within the boundary layer. The $R_{v'p'}$ correlation results for the porous 25 PPI trailing edge remains almost zero within the boundary layer, particularly in the near the trailing edge locations, which indicates the suppression of the flow acceleration and flow vertical movement. This also shows that the surface pressure at the trailing edge location is mainly dominated by the flow boundary layer and perhaps the hydrodynamic field developed inside the porous medium [6]. It is worth mentioning here that in all three cases considered here, particularly for the rough porous surfaces, the correlation at the surface is found to be nearly zero. This shows that despite the increase in the energy content of the velocity fluctuations in the near the wall region, as observed in Fig. 10, these structures do not have a strong correlation with the surface pressure exerted on the surface. Therefore, the overall broadband increase in the surface pressure fluctuations is mainly due to (a) the changes to the boundary layer structures away from the surface and (b) the emergence of the internal hydrodynamic field in the case of highly permeable porous media [6].

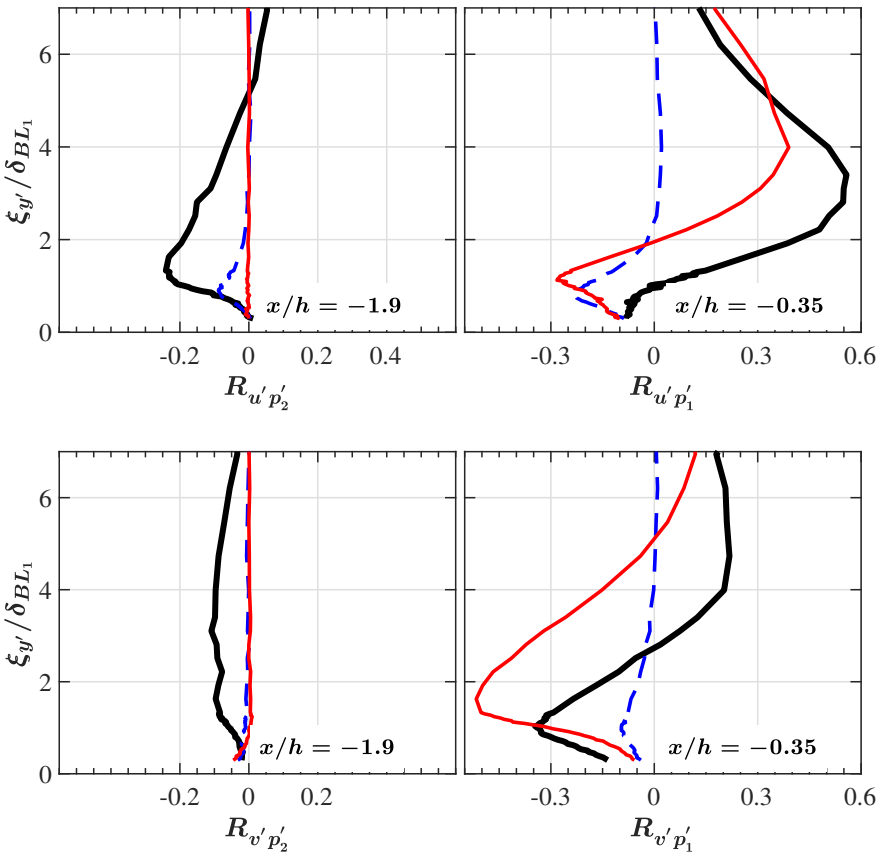

Figure 16: Velocity-pressure correlation components, $R_{u'p'}$ and $R_{v'p'}$ at different streamwise locations over the blunt trailing edge. *Solid trailing edge (—), Porous 80 PPI trailing edge (—), Porous 25 PPI trailing edge (- - -).*

5. Conclusion

The acoustic characteristics of a flat plate with a blunt trailing edge has been considered in this study. The effects of the application of porous trailing edges as a passive method for the reduction of the radiated noise have been investigated. Results have shown that the use of porous trailing edges can effectively eliminate the vortex shedding tonal peaks and also the broadband noise of the plate, leading to a significant noise reduction of about 35 dB using a highly permeable material. A significant part of this noise reduction is due to the elimination of the vortex shedding, as a result of the delay in flow recirculation caused by the porous treatment. The results also clearly show that the porous trailing edges reduce the overall sound pressure level over the entire polar angles for all the flow velocities measured. The near-field to far-field results have shown that the highly permeable materials are able to eliminate the vortex shedding peak entirely and exhibit an almost zero near-field to far-field coherence level. Results have also shown that porous treatments can significantly delay the flow recirculation region, reduce the flow acceleration over the trailing edge, stabilize the flow over the blunt trailing edge and reduce the turbulent production and dissipation within the wake region.

Acknowledgment

The authors would like to acknowledge the financial support from Embraer S.A.

References

[1] M. Szőke, M. Azarpeyvand, Active flow control methods for the reduction of trailing edge noise, in: 23rd AIAA/CEAS Aeroacoustics Conference, AIAA 2017-3004.

[2] M. Szőke, D. Fiscaletti, M. Azarpeyvand, Effect of inclined transverse jets on trailing-edge noise generation, Physics of Fluids 30 (8) (2018) 085110.

[3] B. Lyu, M. Azarpeyvand, S. Sinayoko, Prediction of noise from serrated trailing edges, Journal of Fluid Mechanics 793 (2016) 556–588.

[4] B. Lyu, M. Azarpeyvand, On the noise prediction for serrated leading edges, Journal of Fluid Mechanics 826 (2017) 205–234.

[5] X. Liu, H. Kamliya Jawahar, M. Azarpeyvand, R. Theunissen, Aerodynamic performance and wake development of airfoils with serrated trailing-edges, AIAA Journal 55 (11) (2017) 3669–3680.

[6] S. A. Showkat Ali, M. Azarpeyvand, C. R. I. da Silva, Trailing-edge flow and noise control using porous treatments, Journal of Fluid Mechanics 850 (2018) 83–119.

[7] S. A. Showkat Ali, M. Azarpeyvand, M. Szőke, C. R. Ilário da Silva, Boundary layer flow interaction with a permeable wall, Physics of Fluids 30 (8) (2018) 085111.

[8] S. A. Showkat Ali, M. Azarpeyvand, C. R. Ilario da Silva, Experimental study of porous treatment for aerodynamic and aeroacoustic purposes, in: 23rd AIAA/CEAS Aeroacoustics Conference, AIAA 2017-3358.

[9] S. A. Showkat Ali, X. Liu, M. Azarpeyvand, Bluff body flow and noise control using porous media, in: 22nd AIAA/CEAS Aeroacoustics Conference, AIAA 2016-2754.

[10] A. Afshari, M. Azarpeyvand, A. A. Dehghan, M. Szoke, Trailing edge noise reduction using novel surface treatments, in: 22nd AIAA/CEAS Aeroacoustics Conference, AIAA 2016-2384.

[11] H. K. Jawahar, Q. Ai, M. Azarpeyvand, Experimental and numerical investigation of aerodynamic performance for airfoils with morphed trailing edges, Renewable Energy 127 (2018) 355–367.

[12] M. Choudhari, M. R. Khorrami, Computational study of porous treatment for altering flap side-edge flow field, in: Proceedings of the 9th AIAA/CEAS Aeroacoustic Conference and Exhibit, AIAA 2003-3113.

[13] M. R. Khorrami, M. M. Choudhari, Application of passive porous treatment to slat trailing edge noise, NASA Technical Report 212416 (2003).

[14] A. Bohn, Edge noise attenuation by porous-edge extensions, in: 14th Aerospace Sciences Meeting, 1976, p. 80.

[15] M. R. Fink, D. A. Bailey, Airframe noise reduction studies and clean-airframe noise investigation, NASA Contractor Report 159311 (1980).

[16] J. D. Revell, H. L. Kuntz, F. J. Balena, C. Horne, B. L. Storms, R. P. Dougherty, Trailing-edge flap noise reduction by porous acoustic treatment, 3rd AIAA/CEAS Aeroacoustics Conference, AIAA 1997-1646.

[17] D. Angland, X. Zhang, N. Molin, Measurements of flow around a flap side edge with porous edge treatment, AIAA Journal 47 (7) (2009) 1660–1671.

[18] M. Herr, A noise reduction study on flow-permeable trailing-edges, in: Proceedings of the 8th ONERA-DLR Aerospace Symposium (ODAS) Conference. H. P. Kreplin, Gottingen, Germany, 2007.

[19] T. Geyer, E. Sarradj, Trailing edge noise of partially porous airfoils, in: Proceedings of the 20th AIAA/CEAS Aeroacoustic Conference and Exhibit. Atlanta, GA. AIAA 2014-3039, 2014.

[20] H. Liu, J. Wei, Z. Qu, The interaction of porous material coating with the near wake of bluff body, Journal of Fluids Engineering 136 (2) (2014) 021302.

[21] H. Liu, M. Azarpeyvand, J. Wei, Z. Qu, Tandem cylinder aerodynamic sound control using porous coating, Journal of Sound and Vibration 334 (2015) 190–201.

[22] Y. Bae, Y. E. Jeong, Y. J. Moon, Effect of porous surface on the flat plate self-noise, in: Proceedings of the 15th AIAA/CEAS Aeroacoustics Conference. Miami, Florida. AIAA-2009-3311, 2009.

[23] S. R. Koh, M. Meinke, W. Schröder, B. Zhou, N. R. Gauger, Impact of permeable surface on trailing-edge noise at varying lift, in: Proceedings of the 23rd AIAA/CEAS Aeroacoustics Conference. Denver, Colorado. AIAA 2017-3497, 2017.

[24] S. R. Koh, M. Meinke, W. Schröder, Numerical analysis of the impact of permeability on trailing-edge noise, Journal of Sound and Vibration 421 (2018) 348–376.

[25] A. Vathylakis, T. P. Chong, J. H. Kim, Design of a low-noise aeroacoustic wind tunnel facility at brunel university, in: 20th AIAA/CEAS Aeroacoustics Conference, AIAA 2014-3288.

[26] T. Chong, P. Joseph, P. Davies, Design and performance of an open jet wind tunnel for aero-acoustic measurement, Applied Acoustics 70 (4) (2009) 605–614.

[27] W. K. Blake, Mechanics of Flow-Induced Sound and Vibration V2: Complex Flow-Structure Interactions, Elsevier Science, London., 2012.

[28] G. M. Ozkan, H. Akilli, Flow control around bluff bodies by attached permeable plates, Int. J. Mech. Aerosp. Ind. Mechatron. Eng. 8 (5) (2014) 1035–1039.

[29] C. H. Bruneau, I. Mortazavi, Numerical modelling and passive flow control using porous media, Computers & Fluids 37 (5) (2008) 488–498.

[30] J. E. J. Dupuit, Etudes theoriques et pratiques sur le mouvement des eaux dans les canaux decouverts eta travers les terrains permeables, Second edition, Dunod, 1863.

[31] B. Efron, R. J. Tibshirani, An introduction to the bootstrap: monographs on statistics and applied probability, vol. 57, New York and London: Chapman and Hall/CRC (1993).

[32] G. M. Corcos, Resolution of pressure in turbulence, Journal of Acoustical Society of America 35 (2) (1963) 192–199.

[33] S. P. Gravante, A. M. Naguib, C. E. Wark, H. M. Nagib, Characterization of the pressure fluctuations under a fully developed turbulent boundary layer, AIAA Journal 36 (10) (1998) 1808–1816.

[34] B. H. Timmins, B. L. Smith, P. P. Vlachos, Automatic particle image velocimetry uncertainty quantification, in: ASME 2010 3rd Joint US-European Fluids Engineering Summer Meeting collocated with 8th International Conference on Nanochannels, Microchannels, and Minichannels, American Society of Mechanical Engineers, 2010, pp. 2811–2826.

[35] P. M. Ligrani, P. Bradshaw, Spatial resolution and measurement of turbulence in the viscous sublayer using subminiature hot-wire probes, Experiments in Fluids 5 (6) (1987) 407–417.

[36] Dantec, Dantec Dynamics StreamWare Pro Installation and User Guide, Vol. 5.10. Dantec Dynamics A/S. Skovlunde, Denmark, 2013.

[37] P. Welch, The use of fast fourier transform for the estimation of power spectra: a method based on time averaging over short, modified periodograms, IEEE Transactions on audio and electroacoustics 15 (2) (1967) 70–73.

[38] A. Rubio Carpio, R. Merino Martínez, F. Avallone, D. Ragni, M. Snellen, S. van der Zwaag, Experimental characterization of the turbulent boundary layer over a porous trailing edge for noise abatement, Journal of Sound Vibration 443 (2019) 537–558.

[39] D. J. Moreau, C. J. Doolan, Flow-induced sound of wall-mounted finite length cylinders, AIAA Journal 51 (10) (2013) 2493–2502.

[40] S. Berg, A. W. Cense, J. P. Hofman, R. M. M. Smits, Flow in porous media with slip boundary condition, Society of Core Analysts. Calgary, Canada. (SCA-2007-13) 10–12.

[41] P. Bearman, Investigation of the flow behind a two-dimensional model with a blunt trailing edge and fitted with splitter plates, Journal of Fluid Mechanics 21 (2) (1965) 241–255.

[42] C. Norberg, LDV-measurements in the near wake of a circular cylinder, ASME Paper No. FEDSM98-521 (1998).

[43] O. Lehmkuhl, I. Rodríguez, R. Borrell, A. Oliva, Low-frequency unsteadiness in the vortex formation region of a circular cylinder, Physics of Fluids 25 (8) (2013) 085109.

[44] P. M. Bevilaqua, Intermittency, the entrainment problem, Aerospace Research Labs Wright-Patterson Air Force Base, Ohio, (ARL Technical Report 1975-0095).

[45] J. O. Hinze, Turbulence, New York, McGraw-Hill, 1975.